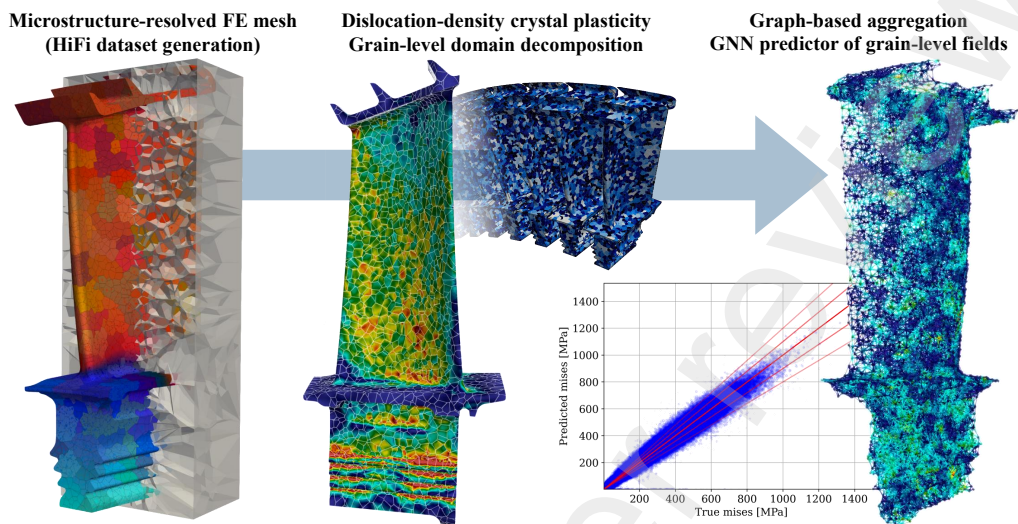


¹ Graphical Abstract

² Full-scale crystal plasticity modeling and data-driven learning of microstructure effects in polycrystalline turbine blades
³ C. Bovet, V. Chiaruttini, A. Vattré



4

5 **Highlights**

6 **Full-scale crystal plasticity modeling and data-driven learning of microstructure effects in polycrystalline turbine blades**
7 C. Bovet, V. Chiaruttini, A. Vattré

- 8
- Full-scale crystal plasticity simulations of a turbine blade with up to 40,000 grains.
 - Interface-aware meshing strategy for embedding realistic microstructures into complex geometries.
 - Dislocation-density based crystal plasticity model including GNDs under finite thermomechanical loads.
 - Grain-wise parallel domain decomposition solved with Adaptive Multipreconditioned FETI (AMPFETI).
 - Graph neural networks trained to predict grain-averaged fields from morphological descriptors.
- 9
- 10
- 11
- 12

13 Full-scale crystal plasticity modeling and data-driven learning of microstructure effects
14 in polycrystalline turbine blades

15 C. Bovet^a, V. Chiaruttini^b, A. Vattré^a

^aOnera, Université Paris-Saclay, 29 av. Division Leclerc, Châtillon, 92320, France

^bDigital Sciences & Technologies, Safran Tech, Magny-Les-Hameaux, 78114, France

16 **Abstract**

A computational framework is developed for full-scale crystal plasticity simulations of polycrystalline Ni-based superalloy turbine blades, explicitly accounting for microstructural heterogeneity. Realistic polycrystalline microstructures with prescribed grain size and orientation are embedded into complex geometries through a conformal meshing procedure, allowing the rapid generation of models with variable grain counts. The constitutive behavior is described by a dislocation-density-based crystal plasticity model incorporating geometrically necessary dislocations under finite deformations and non-isothermal loading conditions. The resulting high-fidelity nonlinear problems are solved using a grain-wise domain decomposition combined with an Adaptive Multipreconditioned FETI solver. The robustness and computational efficiency of the approach with respect to increasing microstructural resolution are demonstrated on a turbine blade geometry containing up to 40,000 grains under representative thermomechanical loading conditions. Finally, the generated simulation database is leveraged to train graph neural networks for predicting grain-averaged mechanical fields from morphological and crystallographic descriptors. The proposed methodology enables systematic investigation of microstructure–property relationships in components with realistic complexity.

17 **Keywords:** Graph Neural Network; mesh intersection; adaptive finite element method; heterogeneity; dislocation density
18 model; crystal plasticity; high performance computing; FETI; polycrystalline turbine blade

19 **1. Introduction**

20 Polycrystalline Ni-based superalloys are extensively employed in aerospace and energy applications due to their exceptional
21 mechanical strength and their ability to withstand severe thermal and mechanical loads. These materials are therefore essential
22 for critical hot-section components such as turbine blades, which operate under high rotational speeds and elevated temperatures.
23 Their mechanical component-scale performance and lifetime are strongly influenced by the underlying microstructure, which is
24 specifically designed to withstand these demanding conditions.

25 In current engineering practice, the macroscopic mechanical behavior and lifetime prediction of these components have
26 mainly relied on numerical simulations using homogenized constitutive relations under service loading (Fedelich, 1999; Cormier
27 and Cailletaud, 2010; Vattré and Fedelich, 2011; Desmorat et al., 2017). Although these approaches offer computational effi-
28 ciency, they often fail to capture local mechanical fields that drive the failure mechanisms, especially in components whose
29 response is strongly influenced by their microstructure. Incorporating microstructural features explicitly in simulations would
30 enable more accurate predictions of local stress and strain concentrations, thus improving the identification of critical regions for
31 damage initiation and growth.

32 High-fidelity modeling efforts have extensively focused on representative volume element (RVE) simulations (Ardeljan et al.,
33 2017; Charpagne et al., 2021; Yan et al., 2021; Demir et al., 2023). These allow for the derivation of macroscopic constitutive
34 laws informed by crystal plasticity, providing a better description of the local intragranular fields that govern fatigue-and creep-
35 driven damage mechanisms. However, transferring this level of fidelity to large-scale simulations of polycrystalline components
36 remains challenging. In particular, RVE-based aggregate calculations do not fully account for the complex local loading arising
37 from component-level geometric nonlinearities. In a finite element context, realistic full-field analysis of heterogeneous materials
38 under service-relevant loading therefore requires advanced meshing strategies capable of embedding multiple microstructural
39 domains with accurate conformity across interfaces into complex geometries while preserving conformal discretizations across
40 grain boundaries and domain interfaces. These challenges motivate the present work.

41 A central bottleneck is the generation of microstructure-informed finite element meshes that can be robustly integrated into
42 full-scale component geometries. At the component scale, the difficulty is not only generating grains, but ensuring geometric
43 validity, conformal interfaces, and mesh quality throughout the full component. Existing tools such as Neper (Quey et al., 2011)
44 and DREAM.3D (Groeber and Jackson, 2014) enable the creation of synthetic microstructures from statistical descriptors and
45 support high-quality meshing at the unit-cell scale. Nevertheless, embedding these microstructures into geometrically complex
46 components, such as full turbine blades, remains an open challenge. Current methods are typically limited to isolated RVEs
47 and do not support robust multi-domain integration while preserving interface conformity, periodicity, and physically consistent
48 boundary conditions. These limitations call for the development of new methodologies capable of generating scalable geometry-
49 aware microstructural meshes suitable for large-scale simulations.

50 In multi-domain settings, adaptive and conformal remeshing techniques must account for intricate geometric partitioning and
51 often rely on specialized treatments to enforce conformity (You et al., 2015; Zhang et al., 2015; Ehab Moustafa Kamel et al.,
52 2019). Recent research has focused on robust intersection of surface meshes, particularly triangulated representations, which is

53 a key step in handling complex microstructural assemblies. Several methods based on mesh arrangements and robust geometric
54 predicates have been proposed to ensure topological and geometric validity (Cherchi et al., 2022; Guo and Fu, 2024; Lévy,
55 2025). However, their performance and robustness in the context of large-scale microstructure generation remain a nontrivial
56 problem for high-resolution microstructures in engineering components. To achieve high-quality tetrahedral meshes compatible
57 with large-scale finite element analysis, constrained Delaunay triangulation algorithms play a central role. Post-processing steps,
58 such as those proposed in Dapogny et al. (2014) enable the improvement of mesh quality while preserving conformity. Efficient
59 and robust tetrahedral meshing methods under geometric constraints, including GPU-accelerated algorithms (Chen and Tan,
60 2019) and the work of Si (2015), have further expanded the scope of feasible configurations.

61 The explicit embedding of the microstructure within the component paves the way for full-field simulations of crystal plas-
62 ticity. Crystal plasticity simulations using Fast Fourier Transforms (FFT)-based solvers provide a computationally efficient
63 framework for heterogeneous polycrystals (Lee et al., 2011; Lebensohn et al., 2012), and several high-performance libraries are
64 available, such as DAMASK (Roters et al., 2019) and AMITEX (Chen et al., 2019). However, FFT-based approaches remain
65 constrained in terms of the geometries they can represent, despite strategies developed to mitigate the inherent periodicity re-
66 quirements (Amadou Sanoko et al., 2025) and handle with conformal internal interfaces (Zecevic, 2026). Two-scale FFT–finite
67 element coupling methods have therefore emerged to combine the efficiency of FFT-based microscale solvers with the geometric
68 flexibility of component-scale finite elements (Gierden et al., 2022). However, these frameworks have only rarely incorporated
69 advanced crystal plasticity formulations, and the most sophisticated demonstrations remain confined to two-dimensional set-
70 tings. Consequently, their current predictive capability for fully three-dimensional path-dependent thermomechanical loading in
71 realistic components remains a challenging problem.

72 In contrast, finite element-based crystal plasticity methods (CP-FEM) (Cailletaud et al., 2003) are not subject to these geo-
73 metric constraints and enable fully resolved, microstructure-informed full-field simulations of complex structures under general
74 boundary conditions. At the component level, Coudon et al. (2020) investigated directionally solidified turbine blades using a
75 coarse-grained, microstructure-explicit representation (with a few grains, only) with a phenomenological constitutive descrip-
76 tion, while Skamniotis et al. (2023) performed a dislocation-based crystal plasticity analysis of fatigue-creep around cooling
77 holes in single-crystal Ni-based blade components. Overall, component-scale analysis combining microstructure-explicit sim-
78 ulations with dislocation-based constitutive models, realistic 3D structural complexity, and boundary conditions that induce
79 highly nonuniform and history-dependent local loading remain scarce in the literature. To the best of the authors’ knowledge,
80 this is the first analysis to perform component-scale, full-field CP-FEM simulations with a dislocation-based constitutive model
81 under complex thermomechanical boundary conditions in a realistic turbine-blade geometry, resolving a very large number of
82 grains and grain boundaries. Beyond capturing the impact of component-level geometric nonlinearities on highly non-uniform
83 local loading paths, the proposed methodology resolves the coupled effect of dislocation-density evolution and grain-boundary
84 interacting on the emergence of microstructure-driven field heterogeneity.

85 In this work, recent developments in mesh generation, dislocation-based crystal plasticity, high performance computing,
86 and graph-based learning are combined into a unified framework for the full-scale simulation of polycrystalline turbine blades.
87 Emphasis is placed on (i) the seamless embedding of realistic multigrain microstructures into component-scale geometries, as
88 well as on (ii) the efficient resolution of the resulting nonlinear boundary-value problems under representative thermomechanical
89 loading. The workflow is introduced through a description of the meshing strategy in section 2, which enables the generation
90 of conformal microstructural discretizations with prescribed grain-size statistics. The constitutive model, based on dislocation
91 density and accounting for geometrically necessary dislocations, is then presented in section 3 and coupled to a domain decom-
92 position solver optimized for grain-wise parallelization, as presented in section 4. Section 5 validates the proposed framework
93 through large-scale simulations of turbine blades with varying grain counts, demonstrating both scalability and predictive capa-
94 bilities. Finally, the resulting database is leveraged to train graph neural networks capable of predicting mechanical fields from
95 microstructural features in section 6, thus opening promising perspectives for surrogate modeling in microstructure-sensitive
96 design.

97 2. Full-scale micro-structural meshing of complex industrial component

98 This section introduces a scalable and robust methodology for embedding heterogeneous microstructures into industrial-
99 scale components, while ensuring conformity along material interfaces. The proposed workflow is compatible with parallel
100 mesh refinement strategies and supports high-quality finite element simulations across multiple material regions. Although the
101 approach is generic and may be extended to various multiscale modeling strategies, it is presented here in the context of full-scale
102 simulations of polycrystalline superalloy turbine blades.

103 The methodology begins with the definition of a homogenized mesh of the structure and proceeds with a sequence of meshing
104 operations that produce a heterogeneous finite element model composed of a prescribed number of material grains.

105 2.1. Seed generation for microstructure discretization

106 While Neper (Quay et al., 2011) provides efficient tessellation capabilities, generating realistic seed distributions inside
107 complex geometries such as turbine blades requires dedicated strategies. Naive approaches based on uniformly seeding the
108 bounding box of the component are highly inefficient: in preliminary trials, less than one-fifth of the generated candidates fell
109 inside the blade, leading to excessive computation times and distorted grain size distributions near free surfaces, where many
110 grains collapsed to unrealistically small volumes.

111 To address these limitations, a tailored seed generation algorithm that directly exploits the finite element mesh of the com-
112 ponent has been developed. Starting from a homogeneous volumetric discretization (typically finer than the target number of

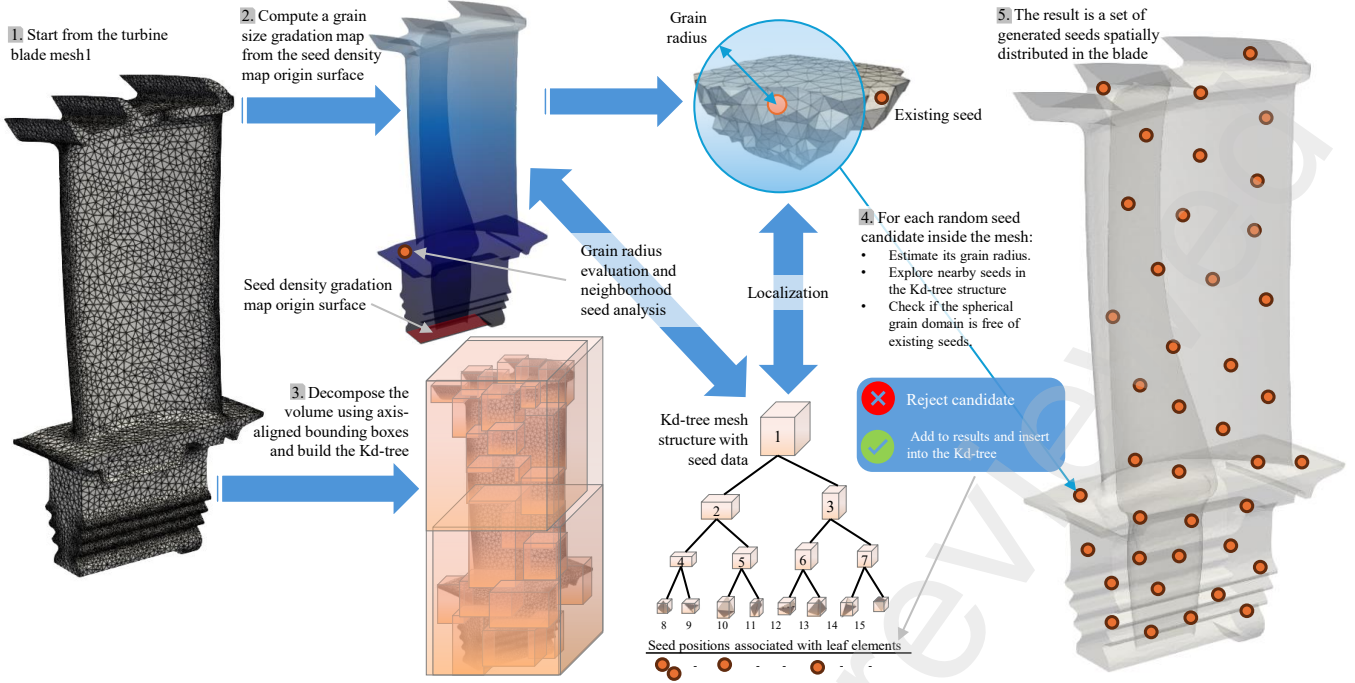


Figure 1: Illustration of the seed generation process using a distance map and k-d tree filtering.

grains) a local grain size field is computed, either uniform or graded (e.g., based on distance to a treated surface). Seed candidates are then generated stochastically and validated through three criteria: (i) localization inside the mesh, (ii) consistency with the prescribed local grain radius, and (iii) absence of overlap with existing seeds. To accelerate this validation, an axis-aligned k -d tree hierarchy is built, enabling efficient neighborhood queries for both grain-size evaluation and collision detection. Accepted seeds are inserted into this structure, ensuring robust spacing and reproducibility.

This algorithm, implemented in multithreaded C++, generates realistic seed populations within seconds even for industrial-scale geometries involving hundreds of thousands of candidates. The resulting seeds are directly compatible with Neper for tessellation, thereby enabling the construction of full-scale polycrystalline microstructures without periodicity assumptions, while accounting for realistic geometrical constraints and boundary conditions. The procedure is summarized in Figure 1, while the following subsections detail the following stages of the meshing procedure.

2.2. Interface-aware mesh extraction and simplification

To simplify the meshing of complex heterogeneous domains, an interface-centric strategy is adopted, based on the observation that only the surfaces separating homogeneous subregions require explicit geometric conformity. This approach significantly reduces the dimensional complexity of the problem while maintaining the ability to reconstruct globally consistent volume discretizations, as illustrated in Figure 2(a).

The initial volumetric mesh is partitioned into subregions \mathcal{E}^j , each associated with a region indicator r^j . Once this partition is defined, interfacial boundaries (i.e., surface elements lying between distinct subregions) are extracted, producing boundary surfaces $\partial\mathcal{E}^j = \mathcal{T}^j$. Duplicate interfaces shared between neighboring regions are removed to ensure that each internal face is uniquely represented.

These filtered interfaces are aggregated into a global set \mathcal{T}_{all} , representing the complete set of inter-region boundaries. To facilitate intersection and conformal remeshing, this surface mesh is converted to a simplicial representation, with quadrilateral or polygonal faces decomposed into linear triangles using standard subdivision algorithms. This interface-aware preprocessing yields a consistent, duplicate-free, simplex-only representation of internal boundaries suitable for robust surface intersection and meshing.

2.3. Surface mesh intersection algorithm

The next stage consists of computing conformal intersections between surface meshes of adjacent regions. This step is essential for constructing shared interfaces that enable consistent volume remeshing. The algorithm proceeds in four parallelizable phases, as illustrated in Figure 2(b).

First, another spatial acceleration structure (k-d tree) is constructed to detect intersecting triangle pairs. For each pair, the geometric intersection contour is computed and stored along with triangle-triangle connectivity and region identifiers in a thread-safe data structure.

Next, for each intersected triangle, a local 2D constrained Delaunay triangulation is performed. The intersection segments are projected into a suitable axis-aligned 2D plane to minimize numerical error, and the triangulation is computed using the open-source library CDT¹, which respects the imposed constraints. The resulting triangles are then mapped back into 3D space. As each triangle is processed independently, this step is highly parallel and scales efficiently.

¹<https://artem-ogre.github.io/CDT/>

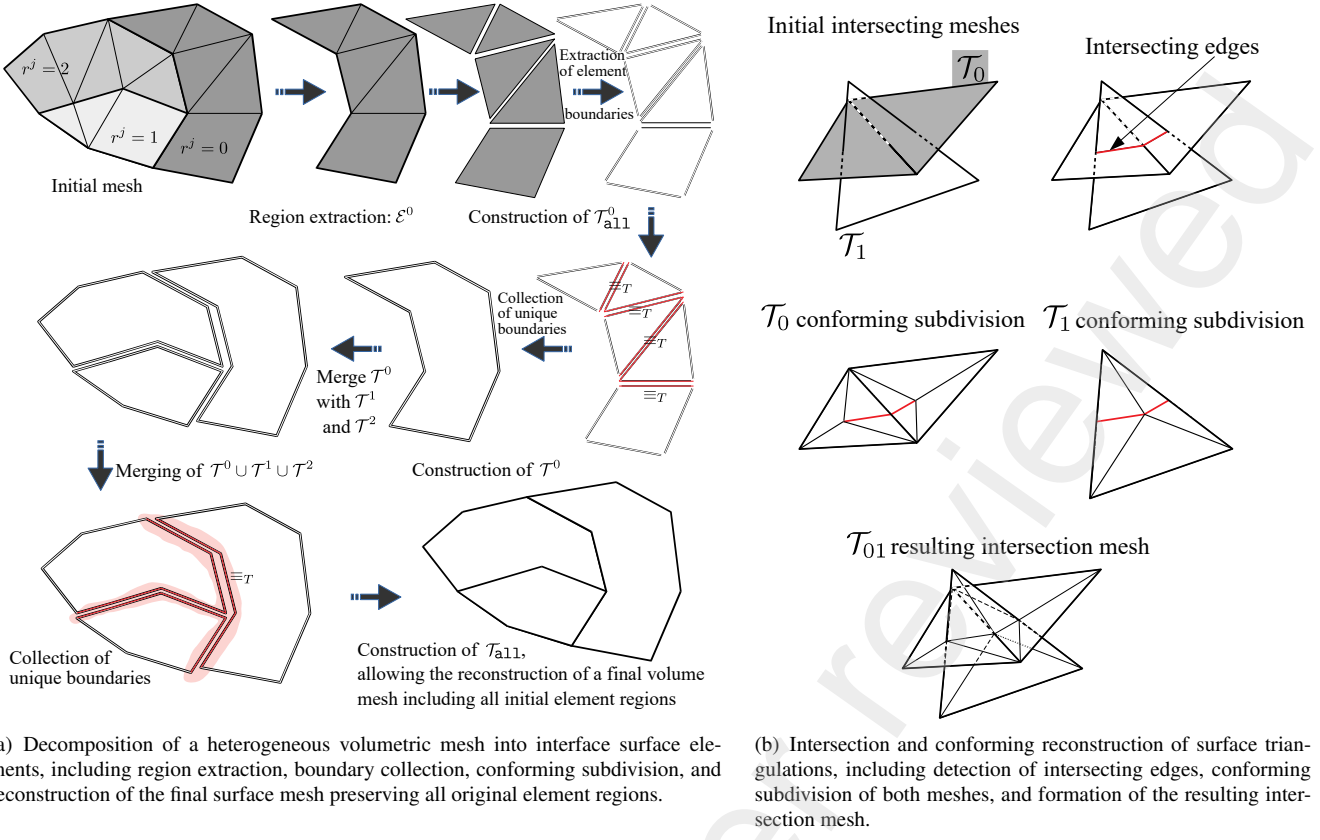


Figure 2: Overview of the main steps involved in mesh decomposition into surface interfaces and in the conforming reconstruction of intersecting triangulations.

148 In a third stage, the resulting surface mesh is optimized through post-processing. Local node merging, edge swapping, and
 149 smoothing techniques are applied to remove poorly shaped elements. Preservation of sharp features is ensured by detecting and
 150 retaining high-curvature edges. After this cleanup process, a high-quality surface mesh, suitable for volume discretization, is
 151 generated using dedicated tools such as `mmg3ds` or `MeshGems SurfOpt`.

152 Finally, a conformal volumetric mesh is reconstructed using the processed interface as boundary input. A constrained De-
 153 launay tetrahedralization is applied (using either `TetGen` or `MeshGems Tetra`) to generate a volume mesh that matches the
 154 conformal surface geometry. Region and interface tags are propagated to the final mesh, ensuring compatibility with numerical
 155 solvers for multi-region simulations.

156 The presented method enables scalable and conformal meshing of heterogeneous domains undergoing local remeshing. The
 157 use of parallel intersection routines, thread-safe connectivity storage, and distance-controlled seed generation ensures compati-
 158 bility with the high-fidelity simulations expected in this analysis. For illustration, Figure 3 demonstrates the capability of the
 159 procedure on a polycrystalline turbine blade containing a 40k-grain microstructure, shown in superposition with the final inter-
 160 sectected finite element mesh.

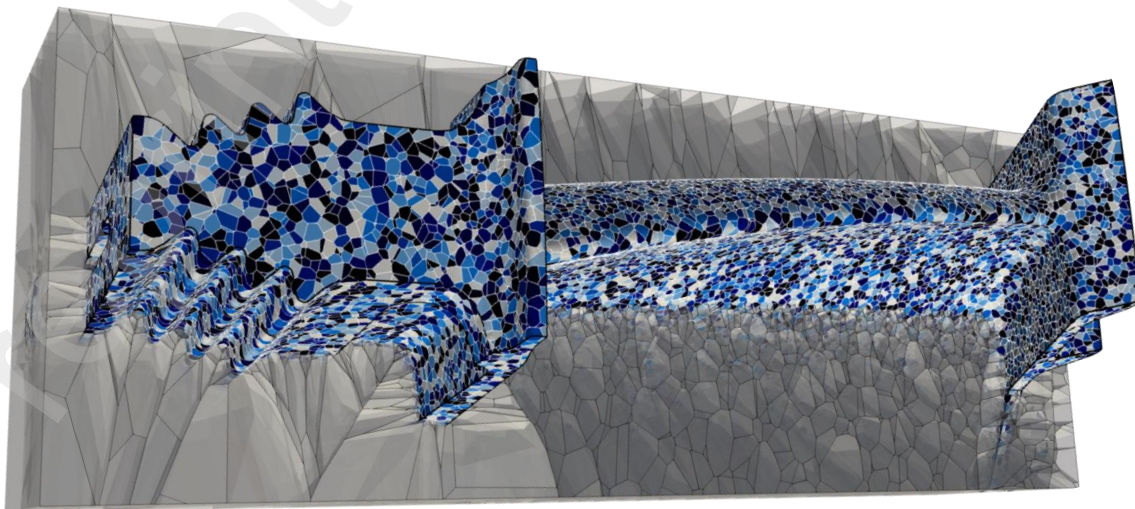


Figure 3: Superposition of the 40k-grain microstructure with the final intersected finite element mesh.

Table 1: Generated microstructure-resolved mesh database. Representative blade views and corresponding mesh characteristics.

Mesh	8k-grain	20k-grain	40k-grain	80k-grain	120k-grain
Preview					
Vertices	1.7M	9.6M	14.8M	54.3M	450M
Tetrahedra	1.1M	6.9M	10.6M	39.8M	334M
Memory per sample	128 MB	700 MB	1.1 GB	3.8 GB	30 GB
Number of sample	16	2	1	1	1

Table 2: Mesh quality histograms for 8k-, 40k-, and 80k-grain meshes.

Mesh	8k-grain		40k-grain		80k-grain	
Worst element quality	406.9		377.2		384.3	
Quality range	Fraction	Count	Fraction	Count	Fraction	Count
1 < Q < 2	73%	415 361	78%	8 327 968	93%	37 174 390
2 < Q < 3	12%	67 221	16%	1 797 393	5%	2 210 064
3 < Q < 4	3%	19 890	2%	317 165	0%	266 351
4 < Q < 5	1%	7 331	0%	103 471	0%	98 080
5 < Q < 10	0%	7 175	0%	87 325	0%	90 459
10 < Q < 100	0%	2 490	0%	15 164	0%	16 480
100 < Q < 1000	0%	103	0%	178	0%	189

Element quality metric: $Q_T = \frac{1}{2\sqrt{6}} \frac{\max_{e \in \mathcal{E}(T)} |e|}{r_{in}(T)}$, where $r_{in}(T)$ is the radius of the inscribed sphere. By construction, $Q_T = 1$ for a regular tetrahedron and larger values indicate increasing element distortion.

162 A database of microstructure-resolved finite element meshes was generated with grain counts ranging from 8k to 120k
163 grains, corresponding to average grain sizes between approximately $740 \mu\text{m}$ and $310 \mu\text{m}$. Depending on the target resolution, the
164 resulting discretizations span from about 1.2 million to more than 450 million vertices, as summarized in Table 1. Representative
165 meshes for each grain count are reported together with their number of vertices and associated memory footprints.

166 Although only meshes containing 8k, 20k, and 40k grains were employed in the simulations reported in this work (with
167 10 realizations at 8k, and one realization each at 20k and 40k grains), the larger meshes at 80k and 120k grains are included to
168 illustrate the scalability of the proposed meshing pipeline and to demonstrate its capability to generate microstructure-conforming
169 discretizations at very high resolutions.

170 As an illustration of mesh quality assessment, Table 2 reports the distribution of the element quality metric Q for the 8k-
171 , 20k-, and 80k-grain meshes. Among these, the 80k-grain mesh represents one of the most challenging cases in terms of
172 mesh size and geometric complexity. More than 93% of its tetrahedra lie in the first quality class, and over 98% exhibit $Q <$
173 3, indicating a globally well-shaped and simulation-ready discretization despite the very large number of elements. While
174 this section focuses on the description of the generated meshes and the discretization strategy, it is worth noting that the few
175 poorly shaped elements present in the largest meshes, with quality values occasionally exceeding $Q > 300$, do not hinder the
176 convergence of the multipreconditioned iterative solver. As demonstrated later in the paper through large-scale simulations, the
177 solver remains robust under such challenging conditions, without requiring explicit element filtering or local remeshing.

178 3. Dislocation-based crystal plasticity model

179 Accurate modeling of the mechanical behavior of polycrystalline superalloys at the microscale requires constitutive laws
180 that capture the fundamental dislocation-mediated mechanisms governing plastic deformation. In this work, a large-deformation
181 crystal plasticity framework is adopted, including the geometrically necessary dislocations (GNDs), which enables the repre-
182 sentation of lattice curvature, slip incompatibilities and intergranular constraint effects. Although shock or impact loading is
183 beyond the scope of the present work, the proposed finite-strain, dislocation-based CP-FEM framework is formulated to remain

applicable under high-strain loading paths relevant to catastrophic scenarios in service, e.g., impact/shock, where strain-rate and temperature effects can critically govern damage and failure (Hou et al., 2002). Another motivation for adopting a dislocation-based formulation is its ability to serve as a foundation for future extensions targeting dynamic strain-aging phenomena. In particular, the present framework is well suited for incorporating mechanisms underlying the Portevin-Le Chatelier effect (Ren et al., 2019), enabling full-field simulations on component-scale structures, where spatio-temporal strain localization may develop under coupled temperature and strain-rate conditions.

In Ni-based polycrystalline turbine blades, plastic deformation is assumed to be governed primarily by dislocation glide on the octahedral slip systems $\{111\} < 110 >$, with climb-controlled mechanisms not included in the present constitutive description. The total deformation gradient \mathbf{F} is multiplicatively decomposed into elastic \mathbf{F}_e , plastic \mathbf{F}_p and thermal \mathbf{F}_T parts (Meissonnier et al., 2001), as follows

$$\mathbf{F} = \mathbf{F}_e \cdot \mathbf{F}_p \cdot \mathbf{F}_T, \quad (1)$$

where \mathbf{F}_p accounts for crystallographic slip. The lattice remains unrotated in the isoclinically relaxed (intermediate) configuration, but thermally-expanded because of the temperature change, only. Thus, the lattice orientation remains unchanged by applying $\mathbf{F}_p \cdot \mathbf{F}_T$.

The mechanical model is considered athermal and decoupled from heat exchanges related to the structure in its environment (no entropy in the present form). Therefore, only a linearized (isotropic) thermal deformation gradient caused by the heat produced by the gases in the engine is taken into account, imposing a heterogeneous temperature field over the entire structure, as described in section 5.1. The thermal deformation gradient is expressed as follows

$$\mathbf{F}_T = (1 + \alpha_T (T - T_0)) \mathbf{I}, \quad (2)$$

where T_0 is the reference/initial temperature of the medium at rest, under the assumption that $|\alpha_T (T - T_0)| \ll 1$, while \mathbf{I} is the second-order identity tensor.

The plastic velocity gradient tensor \mathbf{L}_p that is defined in the intermediate space (Asaro and Rice, 1977) is given by

$$\mathbf{L}_p = \dot{\mathbf{F}}_p \cdot \mathbf{F}_p^{-1} = \sum_{\alpha=1}^{12} \dot{\gamma}^{\alpha} \mathbf{m}^{\alpha} \otimes \mathbf{n}^{\alpha}, \quad (3)$$

with \mathbf{m}^{α} and \mathbf{n}^{α} the slip directions and the normal of the slip planes, respectively. The slip rate $\dot{\gamma}^{\alpha}$ is obtained on the slip system α by virtue of the Orowan equation, i.e.

$$\dot{\gamma}^{\alpha} = \rho_m^{\alpha} b^{\alpha} v^{\alpha} \operatorname{sign}(\tau^{\alpha}), \quad (4)$$

where ρ_m^{α} is the mobile dislocation density, b^{α} is the magnitude of the Burgers vector, v^{α} is the average velocity of the dislocations, and τ^{α} is the resolved shear stress projected onto the slip system α , defined as follows

$$\tau^{\alpha} = \det(\mathbf{F}_T) (\mathbf{F}_T^t \cdot \mathbf{C}_e \cdot \mathbf{S} \cdot \mathbf{F}_T^{-t}) : \mathbf{m}^{\alpha} \otimes \mathbf{n}^{\alpha}, \quad (5)$$

with t the transpose of a tensor, while $\mathbf{C}_e = \mathbf{F}_e^t \cdot \mathbf{F}_e$ is the right elastic Cauchy-Green tensor, and \mathbf{S} is the second Piola-Kirchhoff stress tensor given by

$$\mathbf{S} = \mathbb{C} : \mathbf{E}_e = \frac{1}{2} \mathbb{C} : (\mathbf{C}_e - \mathbf{I}), \quad (6)$$

with \mathbb{C} the fourth-order elastic stiffness tensor and \mathbf{E}_e the corresponding elastic Green-Lagrange tensor.

Since the thermal deformation is small, using eq. (2), the resolved shear stress in eq. (5) reads

$$\tau^{\alpha} = \mathbf{C}_e \cdot \mathbf{S} : \mathbf{m}^{\alpha} \otimes \mathbf{n}^{\alpha}, \quad (7)$$

while the elastic Green-Lagrange tensor can be expressed as

$$\mathbf{E}_e = \frac{1}{2} \mathbf{F}_p^{-t} \cdot \mathbf{F}^t \cdot \mathbf{F} \cdot \mathbf{F}_p - \alpha_T (T - T_0) \mathbf{I}. \quad (8)$$

The rate of the mobile dislocation densities $\dot{\rho}_m^{\alpha}$ for each slip system α is obtained from the generalized storage-recovery relation (Tabourot et al., 1997), i.e.

$$\dot{\rho}_m^{\alpha} = \frac{1}{b^{\alpha}} \left(\frac{1}{\Lambda^{\alpha}} - 2y_c \rho^{\alpha} \right) |\dot{\gamma}^{\alpha}|, \quad (9)$$

which is composed of a positive storage rate term and a negative dynamic recovery term. Here, Λ^{α} is the mean free path associated with elastic interactions among the total dislocation population, defined as the sum of mobile and GNDs contributions, i.e.

$$\rho = \rho_m + \rho_G, \quad (10)$$

218 while y_c is the critical annihilation distance between the dislocations. The mean free path is written in a Taylor-type form as

$$\Lambda^\alpha = \frac{K}{\sqrt{\sum_{\beta=1}^{12} h^{\alpha\beta} \rho^\beta}}, \quad (11)$$

219 where K is a material constant that describes dislocation junction strength, and $h^{\alpha\beta}$ is the slip-interaction matrix accounting for
220 the self-hardening and latent hardening coefficients between dislocations in slip α and β . The GND density ρ_G^β is attributed to the
221 incompatibility of the plastic strain across the grain boundaries, represented by the Nye dislocation tensor (Nye, 1953; Ekkehart,
222 1958) in the intermediate configuration (Arsenlis and Parks, 1999; Ma et al., 2006), as defined by

$$\rho_G^\beta = \frac{1}{b^\beta} \left| (\nabla \times \mathbf{F}_p)^t : (\mathbf{m}^\beta \otimes \mathbf{m}^\beta + \mathbf{m}^\beta \otimes \mathbf{t}^\beta + \mathbf{m}^\beta \otimes \mathbf{n}^\beta) \right|, \quad (12)$$

223 with $\mathbf{t}^\beta = \mathbf{m}^\beta \times \mathbf{n}^\beta$.

224 The velocity of the mobile dislocations is finally obtained by combining both thermally-activated and drag-dominated dislo-
225 cation processes (Frutschy and Clifton, 1998; Austin and McDowell, 2011; Shahba and Ghosh, 2016), as follows

$$v^\alpha = \begin{cases} \frac{\lambda^\alpha}{t_w^\alpha + t_r^\alpha} = \frac{v_d^\alpha}{v_d^\alpha \left(2v_D l^\alpha \frac{b^\alpha}{l_L'^2} \exp\left(-\frac{Q_s^\alpha}{k_B T}\right) \sinh\left(\frac{|t^\alpha| - \tau_A^\alpha}{\tau_T^\alpha}\right) \right)^{-1} + 1} & \text{if } |\tau^\alpha| > \tau_A^\alpha, \\ 0 & \text{otherwise,} \end{cases} \quad (13)$$

226 where $\lambda^\alpha \approx b^\alpha$ is the distance of one Peierls valley, along with t_w^α (Tang et al., 1998) and t_r^α (Hiratani et al., 2003) the average
227 waiting (temporarily arrested by obstacles until the local thermally-activated events occur) and running time of dislocations,
228 respectively, as defined by

$$\begin{aligned} t_w^\alpha &= \frac{1}{2v_D l^\alpha \frac{b^\alpha}{l_L'^2} \exp\left(-\frac{Q_s^\alpha}{k_B T}\right) \sinh\left(\frac{|t^\alpha| - \tau_A^\alpha}{\tau_T^\alpha}\right)}, \\ t_r^\alpha &= \frac{\lambda^\alpha}{v_d^\alpha} = \frac{B_0}{|\tau^\alpha| - \tau_A^\alpha}, \end{aligned} \quad (14)$$

229 with v_D the Debye frequency. In eq. (13), the running time t_r^α is related to the drag-controlled velocity v_d^α as follows

$$v_d^\alpha = \frac{b^\alpha}{B_0} (|\tau^\alpha| - \tau_A^\alpha), \quad (15)$$

230 commonly used in discrete dislocation dynamics simulations (Vattré et al., 2014; Vattré and Chiaruttini, 2022), where the
231 temperature-dependent drag coefficient B_0 is given by

$$B_0 = \frac{c_d k_B T}{v_s b^{\alpha 2}}, \quad (16)$$

232 with c_d the drag constant, k_B the Boltzmann constant, and v_s the shear wave velocity of dislocations (Kocks and Mecking, 2003).
233 On the other hand, l^α in eq. (13) is the average length of the dislocations (Alankar et al., 2011), measured as

$$l^\alpha = \frac{c_l}{\sqrt{\rho^\alpha}}, \quad (17)$$

234 with c_l a material parameter. In addition, l_L^α is the thermally-activated dislocation length needed to move the dislocation lines by
235 passing the Peierls energy landscape, and Q_s^α is the temperature-dependent effective activation energy for dislocation slip that is
236 defined by

$$Q_s^\alpha = Q_0^\alpha + c_q \left(\frac{T}{T_0} - 1 \right)^{p_q}, \quad (18)$$

237 where Q_0^α and T_0 are the reference effective activation energy and temperature, respectively, while c_q and p_q are two materials
238 constants.

239 The athermal resistance τ_A^α to dislocation motion on slip system α is expressed as

$$\tau_A^\alpha = \alpha_A \mu b^\alpha \sqrt{\sum_{\beta=1}^{12} h^{\alpha\beta} \rho^\beta} + \tau_0^\alpha, \quad (19)$$

240 with μ the shear modulus, α_A the statistical dislocation interaction strength constant, and τ_0^α denotes the solute-strengthening
241 contribution to the slip resistance. In the present work, $\tau_0^\alpha = 0$ is set for all slip systems, since the solid-solution effects are

assumed to be negligible compared to forest hardening and GND-mediated strengthening. On the other hand, the thermal resistance τ_T^α is defined by

$$\tau_T^\alpha = \frac{k_B T}{c_a l_L^\alpha b^{\alpha 2}}, \quad (20)$$

with c_a the statistical activation strength constant.

Two asymptotic regimes follow directly eq. (13) for low and high strain rates, namely

i. The thermally-activated regime:

For low strain-rate, i.e., $\tau_r^\alpha \ll \tau_w^\alpha$ in eq. (13), the dislocation velocity expression is reduced to the thermally-activated flow rule, as follows

$$v^\alpha = \begin{cases} \frac{b^\alpha}{\tau_w^\alpha} = 2\nu_D l^\alpha \frac{b^{\alpha 2}}{l_L^{\alpha 2}} \exp\left(-\frac{Q_s^\alpha}{k_B T}\right) \sinh\left(\frac{|\tau^\alpha| - \tau_A^\alpha}{\tau_T^\alpha}\right) & \text{if } |\tau^\alpha| > \tau_A^\alpha, \\ 0 & \text{otherwise.} \end{cases} \quad (21)$$

ii. The drag-dominated regime:

On the other hand, for high strain-rate, i.e., $\tau_w^\alpha \ll \tau_r^\alpha$, the drag is linearly dominated as follows

$$v^\alpha = \begin{cases} \frac{b^\alpha}{\tau_r^\alpha} = v_d^\alpha = \frac{b^\alpha}{B_0} (|\tau^\alpha| - \tau_A^\alpha) & \text{if } |\tau^\alpha| > \tau_A^\alpha, \\ 0 & \text{otherwise.} \end{cases} \quad (22)$$

The details of the constitutive update and the corresponding numerical solution procedure are reported in Appendix A. The appendix provides the local nonlinear integration scheme for the thermo-elasto-plastic decomposition and the associated stress update at the material-point level. This separates the constitutive integration from the global parallelized Newton solve used to enforce equilibrium in section 4.

In addition, within the finite-element solution procedure based on quadratic tetrahedral elements, a regularization length is introduced for the numerical evaluation of the curl of the plastic deformation gradient \mathbf{F}^P . The latter is computed from Gauss-point values using a multithreaded moving least-squares (MLS) differentiation procedure, based on a characteristic length of 200 μm and restricted to material points belonging to the same grain. This regularization ensures that the computed geometrically necessary dislocation densities remain essentially independent of the mesh size, provided that the elements are sufficiently small to properly support the MLS reconstruction.

Overall, all model parameters and their numerical values are listed in Tab. 3, including five dimensionless parameters, which have been used to calibrate the constitutive response of Inconel 718. Temperature-dependent tensile data reported by Special Metals Corp. are adopted as macroscopic benchmarks for cast Inconel 718. Prior to calibration, the representativeness of the chosen RVE was verified by comparing its grain-size population with that of the multiscale blade meshes, as shown in Figs. 4(a)–(b), confirming that the selected 200-grain aggregate adequately captures the targeted statistical distribution.

The calibration is intentionally performed at high temperature (approximately 1088 K, close to the maximum operating temperature of the blade) and is conducted on a statistically representative polycrystalline aggregate containing 200 grains, with an average grain size of 575 μm (discretized into 34k elements and 144k dofs, see Fig. 4(c)), using volume-averaged stress/strain measures. The resulting parameter set is subsequently evaluated at room temperature to assess the model robustness outside the calibration range. For the elastic and thermal properties listed in Tab. 3, linear temperature interpolations are assumed between room temperature and 1198 K.

Figure 4(c) shows the macroscopic uniaxial stress-strain responses at room temperature and at $T = 1088$ K predicted by the dislocation-based crystal plasticity model. As expected, the curves clearly exhibit thermal softening, arising from the temperature-sensitive constitutive parameters.

It is further noted that the grain-size variability relevant to the present component (ranging from approximately 460 to 740 μm) does not induce any significant change in the predicted macroscopic stress-strain response. Within this relatively narrow size range, the aggregate-level mechanical behaviour remains effectively invariant, such that no additional grain-size-dependent parameter identification is required for the purposes of the present study.

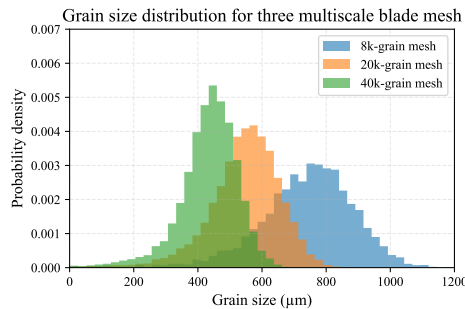
At 1088 K and large deformation, the predicted macroscopic stress at 15% elongation differs from the experimental tensile strength by approximately 0.3%. The responses at all other temperatures follow directly from the temperature dependence embedded in the dislocation-based formulation. In particular, at room temperature, the same model predicts ~ 1343 MPa at 21% elongation, compared with the experimental tensile strength of 1365 MPa, i.e., a conservative deviation of $\sim 1.6\%$. Importantly, the overall thermal softening trend is well reproduced: the experimental reduction in tensile strength from room temperature to 1077 K is $\sim 47.0\%$, while the uniform aggregate prediction yields $\sim 46.0\%$, corresponding to a discrepancy of only $\sim 2.1\%$.

This baseline calibration is sufficient for the methodological objectives of the present work (namely, microstructure-resolved component-scale simulations and solver scalability) and can be straightforwardly refined in future studies using richer datasets and automated multi-objective inverse identification strategies.

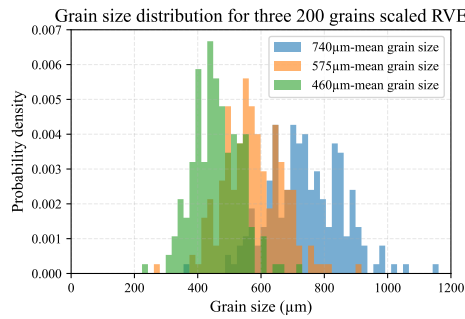
¹Inconel 718 Technical Data Sheet. Available online: <https://www.specialmetals.com/documents/technical-bulletins/inconel-inconel-alloy-718.pdf> (accessed July 2025).

Parameter	Symbol	Value	Dimension
<i>Linear temperature-dependent thermal coefficient</i>			
At room temperature T_0	α_T	4.95×10^{-6}	K^{-1}
At $T = T_0 + 1198 \text{ K}$	α_T	14.68×10^{-6}	K^{-1}
<i>Linear temperature-dependent elastic components</i>			
At room temperature T_0	c_{11}	259.6	GPa
	c_{12}	179.0	GPa
	c_{44}	109.6	GPa
At $T = T_0 + 1198 \text{ K}$	c_{11}	40.2	GPa
	c_{12}	27.7	GPa
	c_{44}	17.0	GPa
<i>Fundamental constants</i>			
Debye frequency	ν_D	9.13×10^{13}	s^{-1}
Boltzmann constant	k_B	1.38×10^{-23}	J K^{-1}
<i>Dislocation-based hardening parameters</i>			
Initial dislocation density	ρ_0^α	10^{12}	m^{-2}
Burgers vector magnitude	b^α	2.57×10^{-10}	m
Critical annihilation distance	y_c	2.57×10^{-9}	m
Dislocation junction strength	K	40	—
Slip-interaction coefficients	$h^{\alpha\beta}$	$h_0 = \dots = h_5 = 1$	—
Statistical dislocation interaction strength constant	α_A	0.3	—
<i>Drag regime</i>			
Shear wave velocity of dislocations	v_s	3500	m s^{-1}
Drag constant	c_d	10	—
<i>Thermally-activated regime</i>			
Thermally-activated dislocation length (Peierls bypass)	l_L^α	5.14×10^{-9}	m
Reference activation energy	Q_0^α	2.9×10^{-19}	J
Reference temperature	T_0	298	K
Activation energy	c_q	6.5×10^{-20}	J
Fraction parameter (average dislocation length)	c_l	2	—
Statistical activation strength constant	c_a	1.32	—
Activation energy exponent	p_q	1.1	—

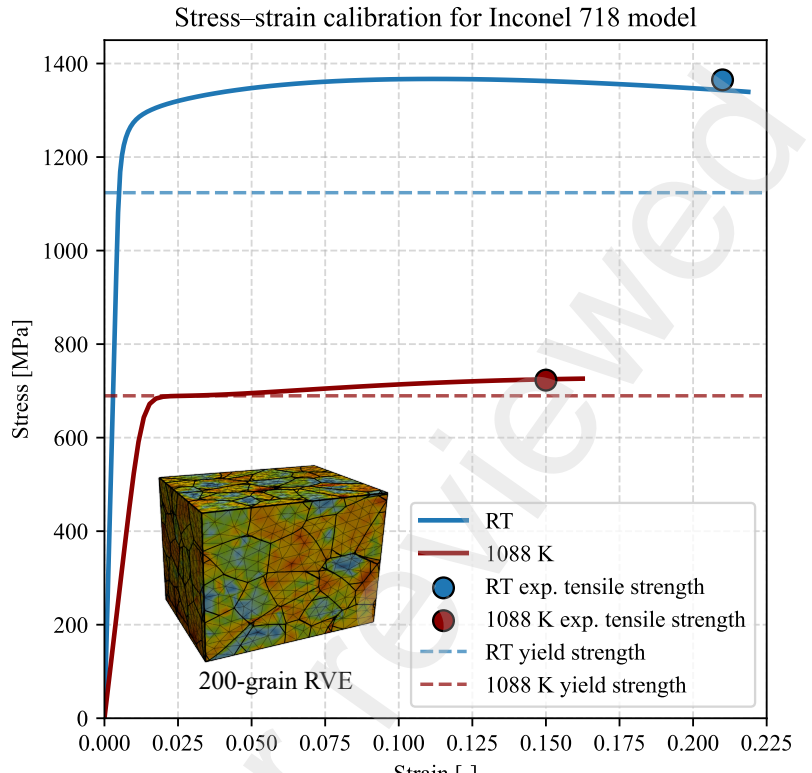
Table 3: Parameters of the dislocation-based crystal plasticity model.



(a) Grain-size distribution in the generated multiscale blade meshes.



(b) Grain-size distribution in the RVE meshes used for calibration.



(c) Identified stress-strain curves at room temperature and 1088 K.

Figure 4: Comparison between the grain-size distributions of the generated blade and the RVE calibration meshes, together with the identified stress-strain responses at room temperature and 1088 K.

288 4. Massively parallel domain decomposition framework

289 Because the previous dislocation-based constitutive update requires a local Newton iteration for dozens of internal variables
290 at every quadrature point, the overall runtime is dominated by repeated nonlinear material-point solves. This motivates the
291 scalable parallel framework used here to make microstructure-resolved component simulations tractable. To enable the high-
292 fidelity simulations presented in this work, a scalable and robust parallel computing framework is required. The computational
293 framework relies on a hybrid parallelization strategy that combines shared-memory and distributed-memory paradigms to ensure
294 efficiency and scalability across modern supercomputers. The finite element mesh is partitioned into subdomains, each assigned
295 to a MPI task, while OpenMP threads are employed within each task to accelerate local operations.

296 4.1. Grain-by-grain domain decomposition

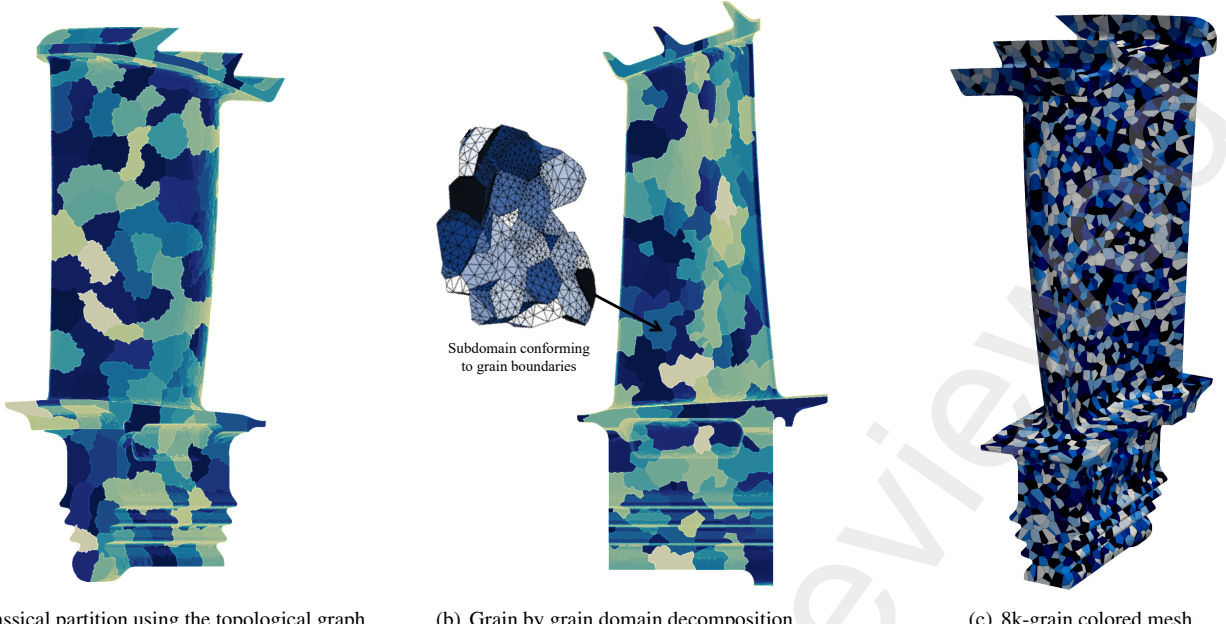
297 The domain decomposition is classically computed using an automatic graph partitioning library such as Metis² or Scotch³.
298 The graph considered is defined by the topology of the mesh \mathcal{G} : graph vertices are the finite elements of the mesh $(e_i)_i$. There is
299 an edge between two vertices if they share a node (or a face).

300 The explicit description of the microstructure in the mesh suggests the use of a more specific domain decomposition where
301 each grain is fully included in only one subdomain. This approach presents two main advantages. First, the domain decom-
302 position interface follows the material heterogeneity which facilitates the convergence of the iterative solver when a stiffness
303 scaling is used (Rixen and Farhat, 1999). Then, all grain-by-grain pre/post processing will be embarrassingly parallel using such
304 a domain decomposition. The computation of $\nabla \times \mathbf{F}_p^t$, required by the material law in eq. 12, becomes local to a subdomain with
305 such a tailored domain decomposition.

306 However, this grain-wise domain decomposition must still minimize the interface size and be well balanced. This is done by
307 coarsening the topological graph \mathcal{G} before calling the graph partitioning library. From the graph \mathcal{G} , a reduced weighted graph
308 \mathcal{G}_g is built, where the vertices are the grains $(g_i)_i$ (identified as a group of elements) and there is an edge between two grains
309 if they share a face. Since the number of elements in a grain is highly variable, it is essential to define appropriate vertex and
310 edge weights to obtain a well-balanced partition. The vertex weight is simply the number of elements of the corresponding
311 grain : $\omega(g_i) = \text{card}(\{e \in g_i\})$. The weight of the edge between two grains (g_i, g_j) is the cut of the corresponding bipartition
312 in the topological graph: $\omega(g_i, g_j) = \text{card}(\{(e_k, e_l) / e_k \in g_i, e_l \in g_j\})$. Figure 5 illustrates the difference between classical and
313 grain-wise domain decompositions.

²<https://github.com/KarypisLab/METIS>

³<https://gitlab.inria.fr/scotch/scotch>



(a) Classical partition using the topological graph.

(b) Grain by grain domain decomposition.

(c) 8k-grain colored mesh.

Figure 5: Illustration of the two kinds of domain decomposition on a 8k grains microstructure mesh (192 subdomains).

314 4.2. Adaptive Multipreconditioned FETI

315 Adaptive Multipreconditioned FETI (Gosselet et al., 2015; Bovet et al., 2017, 2021) (AMPFETI) is used as a linear solver
 316 for the successive tangent linear systems. AMPFETI is the combination of the FETI decomposition method (Farhat and Roux,
 317 1991) with the Adaptive Multipreconditioned Conjugate Gradient (Spillane, 2016). In AMPFETI, the additive structure of the
 318 FETI preconditioner is used in order to generate multiple search directions per iteration. In the most advanced version, the
 319 contribution of the subdomains are aggregated based on their connectivity (Bovet et al., 2021) to limit the growth of the search
 320 space. The adaptation strategy is based on the τ -test (Spillane, 2016). At each iteration, a costless criterion determines whether
 321 a simple conjugate gradient iteration would suffice or whether a multipreconditioned iteration is required. AMPFETI has been
 322 implemented in the high performance computing plugin of the finite element suite Z-set⁴ in a previous work. Its scalability has
 323 been proven up to 10,368 cores and 576 millions of unknowns (Bovet et al., 2021).

324 The use of multiple preconditioners provides robustness against material heterogeneity and quasi-incompressibility (induced
 325 by the plastic flow here), but AMPFETI shares a weakness of the original FETI method, which is the computation of generalized
 326 inverses of floating subdomains. In this work, this point is handled using the graph centrality approach proposed in (Bovet,
 327 2022). Regarding the remaining of the FETI setup, the local preconditioner is the Dirichlet one with stiffness scaling and the
 328 saddle-point Projector is the orthogonal one.

329 5. Numerical results on full-scale turbine blades

330 This section is dedicated to the application of the proposed framework to the simulation of a full-scale turbine blade. A
 331 simplified yet realistic thermomechanical loading is first applied to a polycrystalline representation of the component. The
 332 resulting mechanical response is then examined for several microstructures with an increasing number of grains, up to 40,000
 333 grains, in order to assess both the scalability of the framework and its ability to capture grain-scale effects at different levels of
 334 resolution. All simulations performed in this section used the Onera's in-house supercomputer Sator which is a parallel scalar
 335 cluster with 43,600 cores supplied by NEC.

336 5.1. Description of the thermomechanical problem

337 A full-scale free turbine blade, representative of a helicopter engine application in terms of geometric complexity and op-
 338 erating thermomechanical conditions, is subjected to a simplified yet physically realistic thermomechanical loading scenario
 339 designed to mimic a ramp-up to nominal operating conditions. The geometric model, obtained from the GrabCAD repository⁵,
 340 was deliberately selected for its public availability, ensuring full reproducibility and accessibility of the present study. Despite
 341 its open-source origin, the model exhibits a geometrically complex architecture, including a realistic fir-tree root attachment and
 342 a detailed platform region. This geometric complexity is essential to ensure the representativeness of the computed stress fields
 343 in the most critical regions of the blade, where the thermomechanical response is governed by the combined effects of elevated
 344 temperatures, strong thermal gradients, and locally reduced thickness within the airfoil. These features are known to promote
 345 stress concentration and strain localization, and therefore play a key role in assessing the relevance of the simulated mechanical

⁴<http://www.zset-software.com>

⁵Available at <https://cad.grabcad.com/library/turbine-blade--4>

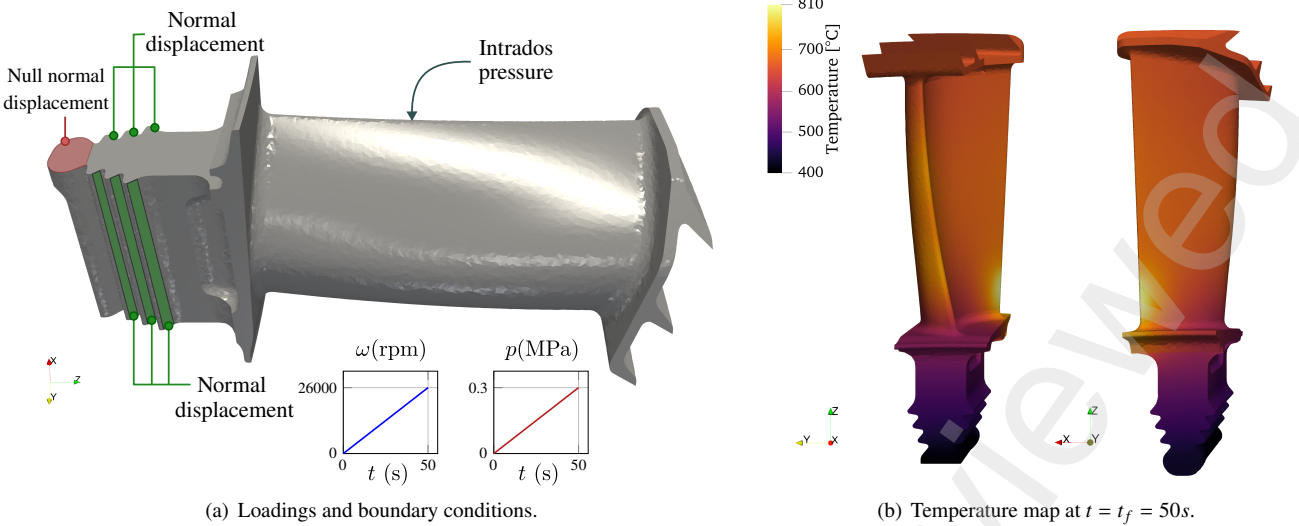


Figure 6: Turbine blade model description.

fields. Although the detailed contact mechanics at the blade–disk interface are not explicitly modeled, the geometric complexity of the root remains essential to capture the resulting stress redistribution under centrifugal loading.

The geometry was uniformly scaled to a total height of 60 mm in order to match the characteristics of an engine delivering approximately 500 kW of power, with a free-turbine diameter of 203 mm. The applied temperature field is not synthetic but results from the transposition of a temperature distribution obtained on an in-service turbine blade, ensuring realistic thermal gradients while preserving industrial confidentiality.

The resulting model is subjected to the boundary conditions illustrated in Figure 6(a). The component is initially considered at room temperature and at rest. The loading is applied over a duration of 50 seconds and involves the following contributions:

- A non-isothermal temperature field, ranging from 400°C to 810°C, is imposed. This field results from a simplified preliminary steady-state heat conduction simulation accounting for thermal exchanges resulting from both external hot gas flow and internal cooling through blade perforations. At $t = 0$, a uniform temperature of 0°C is assumed. A linear temporal interpolation is used between this initial condition and the final temperature map shown in Figure 6(b). The thermal response is computed assuming a homogeneous material, neglecting the influence of the microstructure.
- Displacement constraints are prescribed on the blade root surfaces, representing contact with the turbine disk. Only normal displacements are restricted to prevent any rigid-body motion on the structure.
- A uniform pressure load of 0.3 MPa is applied on the intrados to represent the simplified aerodynamic forces induced by the surrounding pressurized gas.
- Centrifugal forces due to blade rotation at 26,000 rpm are included, using a constant material density of 8,600 kg/m³.

A quasi-static analysis is performed with automatic time-step control to ensure equilibrium throughout the ramp-up. At $t = 50$ s, von Mises stress levels ranging from 400 to 800 MPa are reached in the upper part of the blade. Local overstresses exceeding 1 GPa are observed near the root due to the simplified kinematic constraints. These effects remain confined to colder regions and are not analyzed in detail, as a more accurate treatment would require a full contact model of the blade-disk interface, which lies beyond the scope of this study.

369 5.2. Focus on the 8k microstructure

This section focuses on the results obtained using a microstructure containing 8,000 grains, corresponding to an average grain radius of 0.76 mm. Figure 7 shows the von Mises stress field at $t = 50$ s, with the grain boundaries highlighted for clarity. Highly stressed areas remain mainly defined by mechanical and thermal loads, but the microstructure clearly induces stress concentration at grain boundaries due to grain misorientation. The same applies to the plasticity field defined as

$$\text{Plastic strain} = \sqrt{\mathbf{E}_p : \mathbf{E}_p} \quad \text{where} \quad \mathbf{E}_p = \frac{1}{2} (\mathbf{F}_p^T \cdot \mathbf{F}_p - \mathbf{I}).$$

As shown in Figure 8(a), a diffuse plasticity is visible along the grain boundaries. The maximum value of the color bar has been limited to 10^{-3} to highlight the effect of the grain boundaries more effectively. Most of the plastic flow occurs on surfaces in contact with the disk and at the lower part of the blade where there is a high temperature gradient. One of the qualities of the constitutive model is its ability to differentiate between the plastic flow arising from mobile dislocations (see Figure 8(b)) and the one most due to GNDs (see Figure 8(d)), which are interestingly distributed in different regions of the turbine blade.

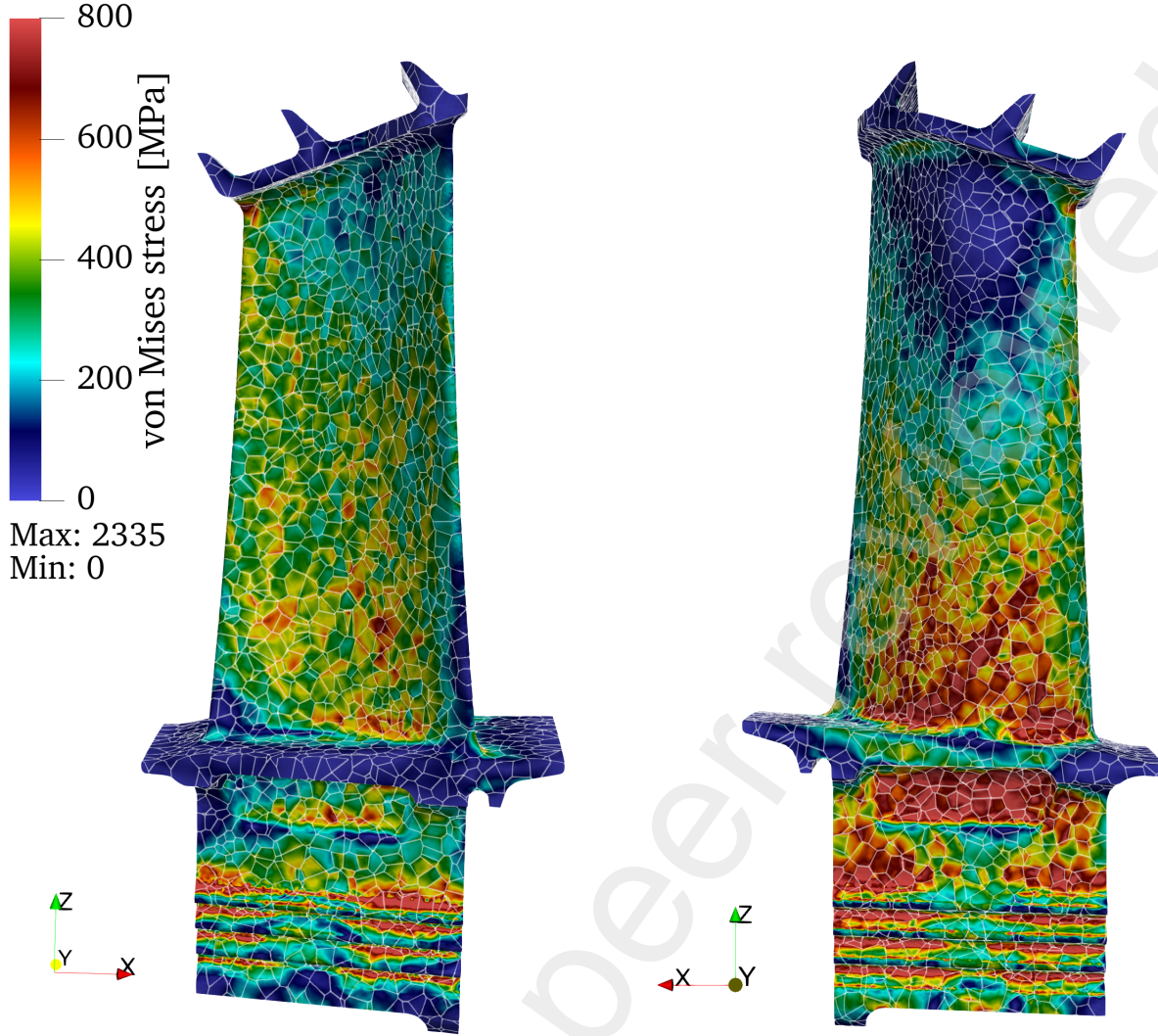


Figure 7: Turbine blade with 8,000 grains: von Mises stress field at $t = t_f$.

379 An important capability of the model is its ability, in a manner consistent with the applied thermomechanical loading, to
 380 analyze the velocity of mobile dislocations and thereby identify whether plasticity proceeds in the thermally activated or drag-
 381 dominated regime. To this end, a scalar measure of the dislocations velocity is defined as the sum of the absolute velocity on all
 382 slip systems:

$$\text{Total velocity} = \sum_{\alpha=1}^{12} |v^\alpha|.$$

383 The total velocity is shown in Figure 8(c), for which the reported values reflect the thermally activated glide of dislocations, as
 384 given by the unified velocity relation under the prescribed boundary conditions.

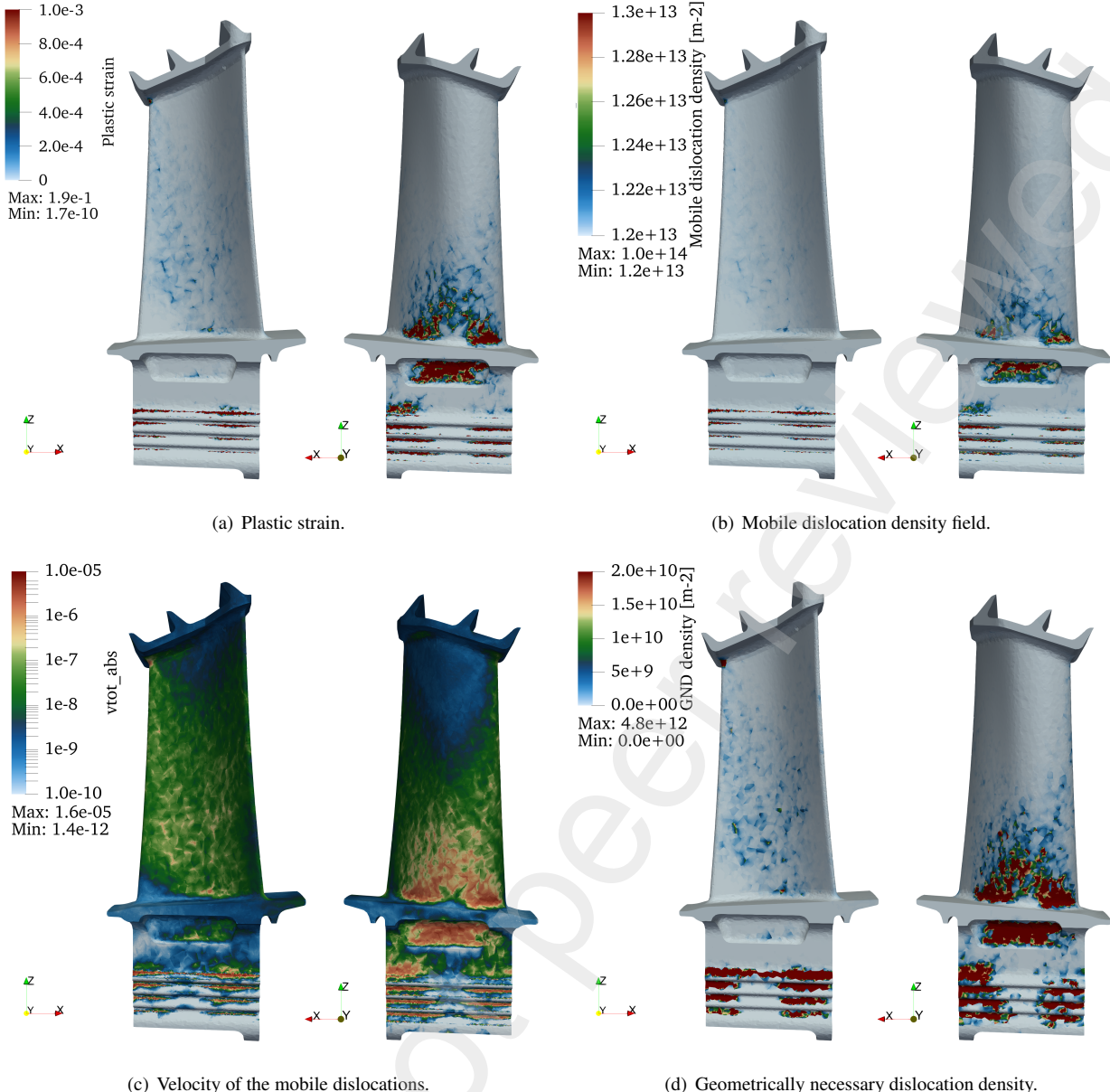


Figure 8: Iso-values for turbine blade with 8,000 grains at $t = t_f$.

5.3. Grain size effects

The same simulation can be extended to microstructures containing a larger number of grains. As the number of grains increases, so does the size of the finite element problem. For instance, a simulation involving 20,000 grains, corresponding to a mean grain radius of 0.56 mm, leads to a system with 28 million degrees of freedom, distributed over 384 cores. The simulation lasts about 4 hours. Similarly, another case with 40,000 grains, corresponding to a mean grain radius of 0.45 mm, results in 45 million degrees of freedom and runs on 480 cores. The simulation lasts about 8 hours. In both cases, the computations remain well within the capabilities of the proposed conformal-mesh, dislocation-based, massively parallel numerical framework.

The von Mises stress field at $t = 50s$ for a microstructure with 20,000 grains is shown in Figure 11(a) and a zoom is provided in Figure 5.3. Similarly, Figure 11(b) shows the von Mises stress field for a microstructure with 40,000 grains. The high-stress regions coincide with those identified for the 8k-grain microstructure. As in the previous configuration, the microstructural influence on the stress field is clearly apparent.

Beyond local fields, global indicators such as the volume-averaged plasticity indicator and the volume-averaged densities of mobile dislocations and GNDs are also of interest. To obtain statistically representative quantities, we performed five simulations for each microstructure, with randomly assigned grain orientations for each realization.

Thanks to the meshing procedure described in Section 2, most of the simulations have been carried out successfully for the 8k, 20k, and 40k-grain microstructures. Only one simulation involving the 20k microstructure, due to a specific grain orientation realization, exhibited local numerical difficulties associated with the large-deformation regime and could not reach the final simulation time of $t = 50s$. Although the initial meshes were carefully generated, a small fraction of elements still exhibited relatively poor quality (with values exceeding a threshold of 100 according to the mesh-quality criterion introduced earlier in Table 2). Such elements are more likely to be present when increasing the number of grains, due to the combined effects of geometric complexity, small characteristic element sizes near grain boundaries, and topological constraints imposed by the

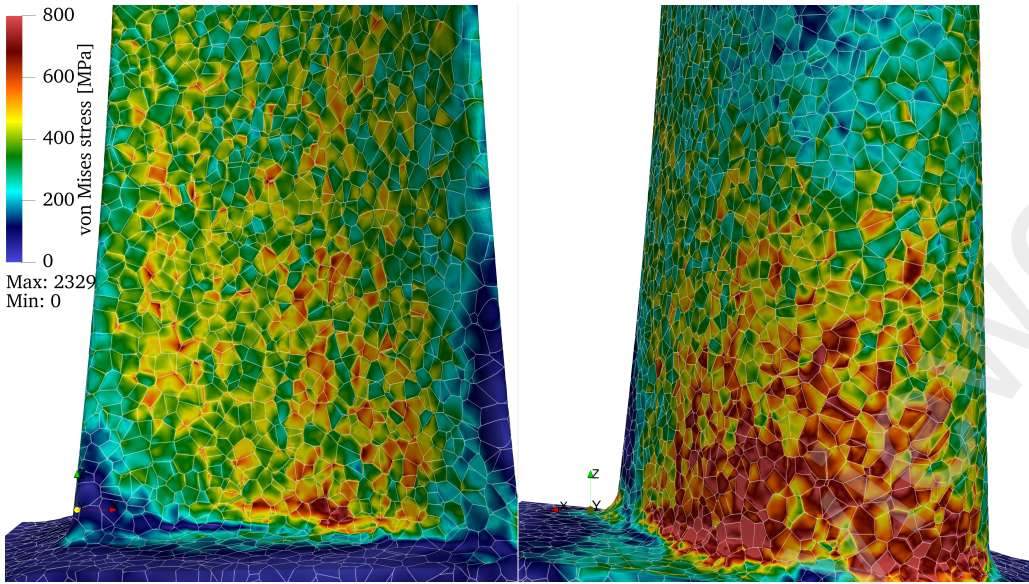


Figure 9: Turbine blade with 20000 grains: local von Mises field at $t = t_f$.

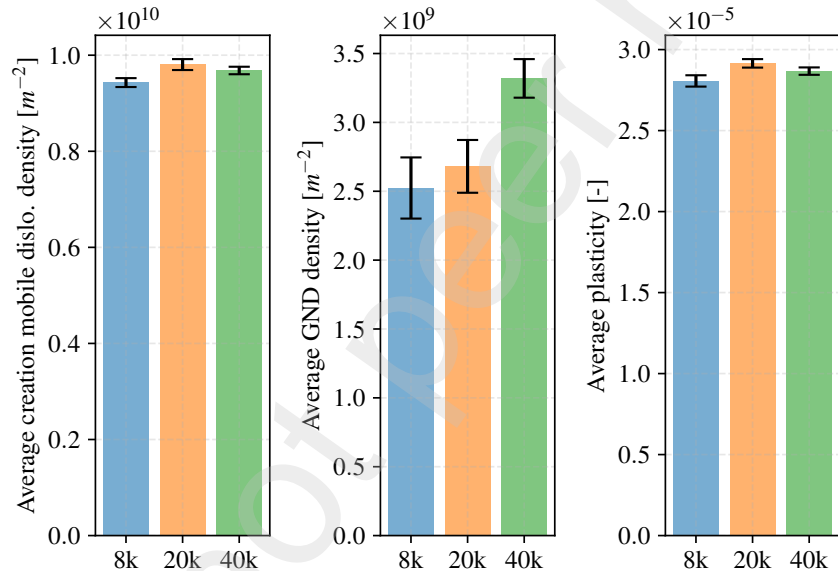


Figure 10: Grain size effect on the plastic indicator and dislocation generation for the three target microstructures (8k, 20k, 40k). Results are averaged over five randomly sampled crystallographic orientations. For the 20k microstructure, one simulation could not reach the final simulation time of $t = 50$ s.

406 polycrystalline tessellation.

407 In the context of finite-strain crystal plasticity, these low-quality elements may experience excessive distortion during the
408 simulation. In particular, they can undergo element inversion, leading to a negative Jacobian determinant and consequently to a
409 breakdown of the constitutive integration. The automatic time-increment control mitigates this issue by reducing the time step
410 when strong nonlinearities are detected. However, in a few cases, this mechanism alone remains insufficient to fully prevent
411 element inversion under highly heterogeneous stress and strain fields induced by grain misorientation.

412 It is important to emphasize that this difficulty cannot be resolved solely by further improving the quality of the initial
413 mesh. Indeed, element inversion is not only a geometric issue, but also a mechanical one, arising from the strong localization
414 of deformation and stress incompatibilities at grain boundaries. A robust resolution of this problem would require on-the-fly
415 mesh adaptation combined with a consistent transfer of internal variables, such as dislocation densities, between successive
416 meshes (Resk et al., 2009; Frydrych et al., 2019). Implementing such a strategy within a massively parallel framework for
417 large-scale polycrystalline simulations remains a challenging task and is beyond the scope of the present work.

418 Nevertheless, the successful completion of a significant number of simulations allows us to analyze and discuss the global
419 indicators of plastic activity. As shown in Figure 10, both the accumulated plastic strain and the density of mobile dislocations
420 exhibit a slight increase as the grain size decreases. This trend is significantly more pronounced for the density of geometrically
421 necessary dislocations, which strongly reflects the enhancement of strain gradients and intergranular incompatibilities in finer
422 microstructures. These observations are consistent with the expected increase in intergranular effects as the number of grains
423 increases. It should be emphasized that the observed grain-size effects are obtained within a relatively limited range of average

424 grain sizes, representative of the considered component and manufacturing route, and should therefore be interpreted with appropriate
 425 caution. Although the observed trends are robust across the present simulations, additional realizations would be required
 426 to fully quantify their statistical significance.

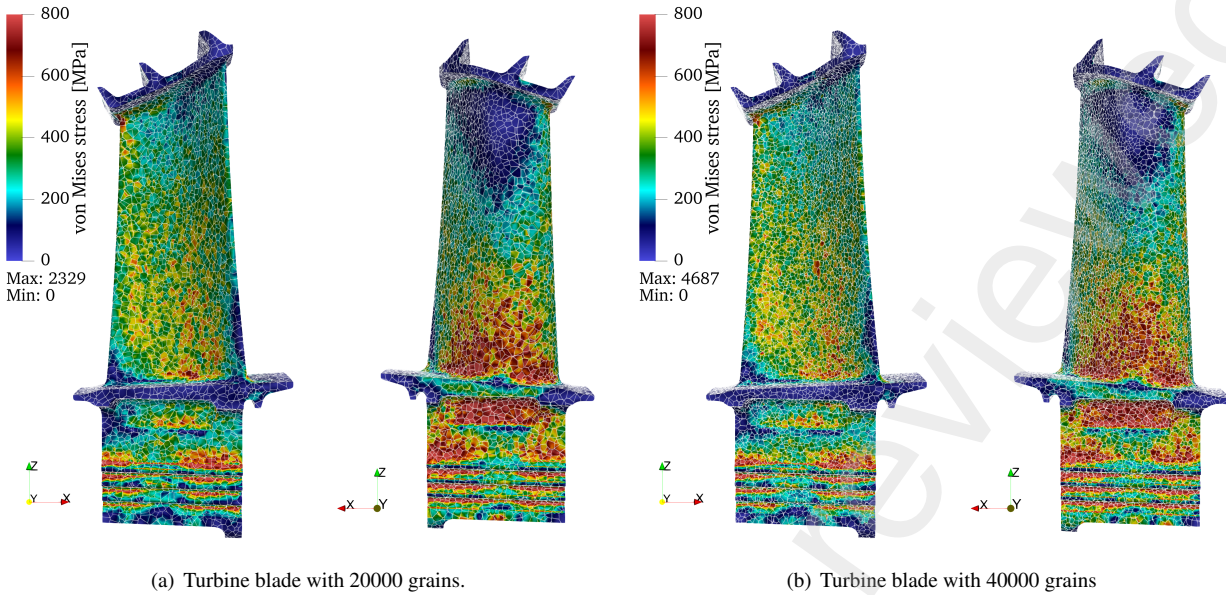


Figure 11: Von Mises stress field at $t = t_f$.

427 6. Toward learning microstructural effects using graph neural networks

428 The previous section proposed a first analysis of the effect of the microstructure on the mechanical response of the blade,
 429 taking into account grain size and grain orientation. This section takes full advantage of these new computational capabilities and
 430 develops a model reduction technique based on graph neural networks. The aim is to predict grain-averaged mechanical values
 431 for unseen microstructures and/or orientations. From a machine learning point of view, this task is a node prediction problem.
 432 Graph neural networks have been successively applied to crystal plasticity finite element models to predict homogenized properties
 433 (Hestroffer et al., 2023), homogenized behavior (Frankel et al., 2022) or local mechanical fields (Gao et al., 2025). However,
 434 these studies only consider RVEs.

435 The complexity of the polycrystalline behavior law does not pose a significant challenge for machine learning algorithms.
 436 Indeed, a plastic model produces more clustered results by alleviating stress concentrations than by considering only cubic
 437 elasticity. To reduce the cost of generating the dataset, we only consider finite strain cubic thermoelasticity in this section. The
 438 developed methodology remains applicable to the crystal plasticity model. The long-term goal may be to provide guidelines for
 439 optimizing the microstructure for a given application (a turbine blade in the present work).

440 6.1. Microstructures as graphs

441 The microstructure of the turbine blade has already been seen as a specific weighted graph in Section 4.1 in order to compute
 442 a grain-by-grain decomposition of the mesh. The same graph \mathcal{G}_g is considered here, where grains are graph vertices and edges
 443 correspond to a common grain boundary, but with totally different nodes and edges features. Indeed, the graph must provide a
 444 reduced description of both the turbine blade (input) and the finite element results (output). An illustration of such a model is
 445 shown in Figure 12.

446 6.1.1. Graph inputs

447 For a given grain g_i , the selected node characteristics are as follows:

- 448 • the position of the gravity center of the grain g_i
- 449 • the volume of the grain $V(g_i)$
- 450 • the orientation of the grain, modeled as the rotation vector $\psi = \mathbf{u}\psi$ where ψ is the rotation amplitude and \mathbf{u} is the unit
 451 vector aligned with the rotation axis.

452 For a given edge (g_i, g_j) , the selected edge features are:

- 453 • the surface of the grain boundary between g_i and g_j
- 454 • the grain boundary normal vector \mathbf{n}^{ij}

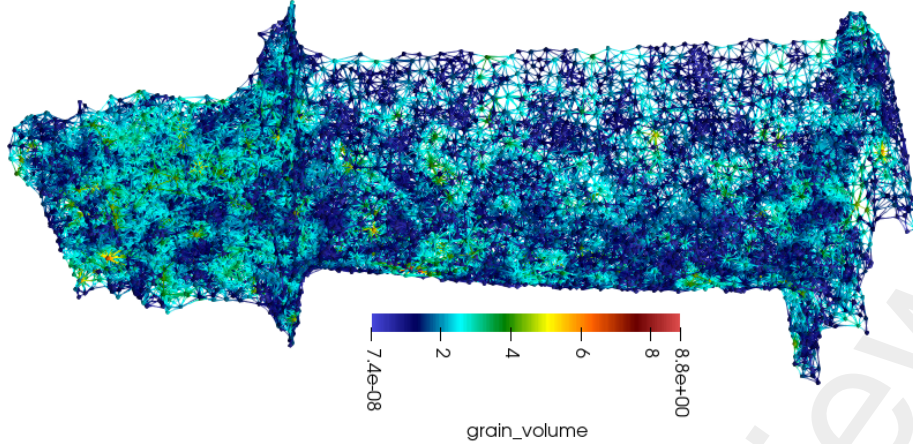


Figure 12: Blade microstructure modeled as a graph: graph vertices are grains and an edge corresponds to a shared grain boundary. The graph contains approximately 8000 grains.

455 Thus, the \mathcal{G}_g is equipped with 7 node features and 4 edge features, which is sufficient to account for grain and grain boundary
 456 morphology and grain misorientation. As the boundary conditions defined in section 5.1 are used in all finite element simulations
 457 of the dataset, this set of features also *indirectly* accounts for the thermo-mechanical load. Indeed, the position of a grain in the
 458 turbine blade defines, to a first order, the temperature and the centrifugal load to which it is exposed. The alignment between the
 459 microstructure and the centrifugal load is also considered through the grain orientations and grain boundary normals.

460 Alternatively, incorporating Schmid factors into node characteristics could be considered, but this would require knowledge
 461 of the mean stress tensor for each individual grain. Given that the predominant load is the centrifugal one, a simplified approach
 462 would be to compute the Schmid factor relative to an uniaxial traction along the z -axis. This approach is not considered further
 463 in this work.

464 6.1.2. Graph outputs

465 The graph output provides reduced representation of the turbine blade finite element results. These outputs are logically
 466 defined per grain. For a given mechanical scalar quantity y , the considered outputs of the node g_i are the average and the
 467 standard deviation:

$$\begin{aligned} \bar{y}_i &= \frac{1}{V(g_i)} \int_{g_i} y(\mathbf{x}) dv \\ S(y_i) &= \sqrt{\left(\frac{1}{V(g_i)} \int_{g_i} y(\mathbf{x})^2 dv \right) - \bar{y}_i^2}. \end{aligned} \quad (23)$$

468 These quantities are computed in practice with the classic Gaussian quadrature at the end of the computation ($t = 50s$). The
 469 mechanical quantities considered in this work are:

- 470 • the component of the stress tensor σ_{ij}
- 471 • the von Mises stress

472 Thus, \mathcal{G}_g is equipped with $2 \times 7 = 14$ node outputs. These outputs are the results that are learned by the GNN. If the crystal
 473 plasticity model defined in Section 3 had been used, the densities of mobile and geometrically necessary dislocations, as well as
 474 the plastic indicator would have been logically included in the graph output.

475 6.2. Description of the two datasets

476 Two datasets are generated, both targeting a microstructure with 8,000 grains. The first dataset, denoted as "(O)" here-
 477 after, considers a single microstructure but utilizes 2,000 random draws of orientations. The second dataset, denoted as "(M)",
 478 considers 10 different microstructures, each with 100 orientation draws.

479 Orientations are randomly sampled from a uniform distribution: the amplitude ψ is uniformly distributed across the interval
 480 $[-\pi, \pi]$ while the direction \mathbf{u} is built normalizing a random draw in \mathbb{R}^3 . Thus, the random draw does not account for the cubic
 481 symmetry of the material law. This will be addressed with a specific pre-transform in Section 6.4.1

482 Blade meshes containing 8,000 grains have approximately 1.7M nodes and 1.2M elements (quadratic tetrahedra). All com-
 483 putations are run on the Sator supercomputer with 192 subdomains. Each simulation lasts approximately 270 seconds. Conse-
 484 quently, generating each dataset requires around 28,800 CPU hours for dataset (O) and 14,400 CPU hours for dataset (M).

485 As observed in Section 5, the computation time for a 8,000 grains simulation using the crystal plasticity law is approximately
 486 3400 seconds (with 192 cores). Consequently, generating datasets (O) and (M) with this law would require around 544,000 CPU
 487 hours. This is entirely feasible since a typical "small" project in a GENCI call is about 1M CPU hours (<https://www.edari.fr/>). However, it would not be reasonable to incur this cost for such a synthetic blade geometry.

489 6.3. Description of the GNN architectures

490 Two GNN architectures are employed to predict the grain-averaged mechanical properties. The first architecture, Graph-
491 SAGE (Hamilton et al., 2018), is known for its ease of training but does not incorporate edge features. The second architecture
492 is based on GENConv layers (Li et al., 2020), which exhibit greater generalization capabilities and incorporate edge features.
493 However, they can be more challenging to train. The objective of this section is not to identify the neural network architecture
494 best suited to our regression problem, but rather to demonstrate the use of state-of-the-art architectures that are readily available
495 in standard AI frameworks such as PyTorch. The search for the optimal neural network architecture is clearly beyond the scope
496 of the present paper.

497 6.3.1. Architecture 1. Graph SAGE

498 The first graph neural network is based on the Graph SAGE architecture (Hamilton et al., 2018). As Graph Sage does not take
499 edge features into account, the inputs are limited to the node features defined in section 6.1.1. The model is made up of 4 message-
500 passing layers, each with a hidden dimensionality of 2048. It uses ReLU activation functions, mean aggregation and batch
501 normalization to enhance numerical stability and convergence. At depth k , the message passing layer (before normalization) is:

$$502 \mathbf{h}_v^k \leftarrow \text{ReLU} \left(\mathbf{W}^k \cdot \left(\text{MEAN} \left(\{\mathbf{h}_u^{k-1}, u \in \mathcal{N}(v)\} \right) \cup \{\mathbf{h}_v^{k-1}\} \right) \right) \quad (24)$$

502 where \mathbf{h}_v^k is the message of the current vertex, $\mathcal{N}(v)$ the direct neighborhood of v and \mathbf{W}^k are the learnable parameters.

503 The number of output features depends on the specific regression task and ranges from 1 to 14. Indeed, one approach consists
504 in training a separate GNN for each component of the graph output defined in section 6.1.2, which simplifies the regression task
505 but neglects potential correlations among the outputs. Alternatively, a single GNN can be trained to simultaneously predict all
506 components of the graph outputs, thereby exploiting their inherent correlations.

507 6.3.2. Architecture 2. GENConv

508 The second graph neural network is based on the GENConv message passing layer (Li et al., 2020). The model is made up
509 of 4 message-passing layers, each with a hidden dimensionality of 1024. We opted for a smaller network width for GENConv
510 for two reasons. Firstly, we wanted the model to fit within the memory of a single A100 GPU for practical reasons. The
511 second reason is to enable a fairer comparison with GraphSAGE: for an equal width, GENConv contains a larger number of
512 parameters due to its use of edge features. As for GraphSage, we opted ReLU activation functions, mean aggregation and batch
513 normalization. At depth k , the message passing layer (before normalization) is:

$$514 \mathbf{h}_v^k \leftarrow \text{ReLU} \left(\mathbf{W}^k \cdot \left(\text{MEAN} \left(\{\text{ReLU}(\mathbf{h}_u^{k-1} + \mathbf{e}_{uv}), u \in \mathcal{N}(v)\} \right) \cup \{\mathbf{h}_v^{k-1}\} \right) \right), \quad (25)$$

514 where \mathbf{e}_{uv} are edge features between vertex u and v . GENConv can also learn activation-function parameters or message-scaling
515 factors, but these capabilities are not used in the present work. GENConv being a node-update-only convolution, edges features
516 are not updated. They remain static descriptors of pairwise relations, which makes them well suited to our node prediction
517 regression task. Grain boundaries orientation and area help the GNN understand how grains are connected.

518 6.3.3. Enforcing positivity of some outputs

519 By construction, certain predicted quantities are strictly positive, such as the von Mises equivalent stress and the standard
520 deviations of the stress tensor components (as well as that of the von Mises stress). To enforce this positivity constraint, a SoftPlus
521 activation function is applied to the output of the final layer. Although a ReLU activation function could also be employed, it
522 suffers from vanishing gradients for negative input values. For this type of regression task, the SoftPlus function is therefore
523 more appropriate.

524 6.4. Some details about training and validation

525 6.4.1. Pre-transform processes

526 To facilitate learning, it is crucial to pre-process the data. Classically, all quantities (node features, edge features, node
527 outputs) are normalized considering the entire dataset using min-max normalization. Additionally, since all data are initially
528 stored in Float64, they are compressed to Float32 to accelerate the learning process.

529 An interesting aspect is the treatment of orientations. During dataset generation, orientations were randomly drawn from the
530 rotation space without considering the cubic symmetry properties of the behavior law. Consequently, two different orientation
531 vectors ψ and ψ_r can lead to the same local physical behavior if they are related by one of the members of their symmetry group.
532 That is:

$$533 \exists \Lambda \in O_h \text{ such that } \mathbf{R}(\psi_r) = \Lambda \cdot \mathbf{R}(\psi), \quad (26)$$

533 where O_h is the Cubic symmetry group. Here, two approaches can be pursued. The first involves enhancing data quality by
534 leveraging physical knowledge of the data. Thus, a specific pre-processing technique is applied, reducing the rotation amplitude
535 while accounting for the cubic symmetries of the law. This essentially means searching for the reduced rotation $\mathbf{R}(\psi_r)$ satisfying
536 eq. (26) such that ψ_r has a smallest magnitude. This approach improves the information content within the data without increasing
537 the dataset size. We implemented this pre-transform process in this work using the `reduce` method from the rotation class
538 `Rotation` provided by `scipy`.

539 Alternatively, this cubic symmetry enables a "dataset augmentation" approach which increases the dataset size without re-
540 quiring additional high-fidelity calculations. Indeed, the graph \mathcal{G}_g^* built from graph \mathcal{G}_g , but where the grain orientations have
541 been composed using member of O_h , represents the same physical calculation. This approach can efficiently augment datasets
542 for ML model training, potentially improving model performance without incurring significant additional computational costs.
543 This data augmentation approach has not been considered further in this work, which prioritizes data quality over quantity.

544 6.4.2. Loss function and optimizer

545 The machine learning project configuration is relatively simple. Both datasets (O) and (M) have been divided into training,
546 validation, and testing sets. For both, the training set contains 90% of the dataset, while both the validation and testing sets each
547 correspond to 5% of the dataset. The loss function is the classical mean squared error (MSE) provided by `torch.nn.MSELoss`
548 while the regression is performed with the Adam adaptive optimizer `torch.optim.Adam`. Both the loss on the training and
549 validation sets are tracked to avoid overfitting.

550 6.4.3. Hardware & software

551 The training and testing of the model in this section were conducted in the Topaze supercomputer which is managed by the
552 French Computing Center for Research and Technology (CCRT, <http://www-ccrt.cea.fr>). Only one GPU NVIDIA A100
553 GPU of AMD Milan nodes is used for both training and validation. The development and implementation of the deep learning
554 model were based on the PyTorch (2.8) and PyTorch Geometric (2.7) deep learning framework.

555 6.5. Regression results for unseen orientation (dataset (O))

556 For the unseen orientation dataset (O), only the node features vary (i.e., the grain orientations), while the edge features remain
557 identical across all graphs in the dataset. Consequently, the benefit of using a GNN that accounts for edge features is limited.
558 Therefore, only the results obtained with GraphSAGE are presented in this section.

559 6.5.1. Training one GNN for the von Mises stress

560 This section applies the first strategy described in section 6.3.1, that is, training a GNN for each component separately. This
561 approach is illustrated in this section for the von Mises equivalent stress, but training a GNN to predict a single component of
562 the stress tensor leads to similar results.

563 *Results obtained with the GraphSAGE architecture.* After 150 epochs, the training loss and the validation loss are 4.269×10^{-5}
564 and 3.92×10^{-5} respectively. The training process takes approximately six hours. The slightly higher training loss can be
565 attributed to the much larger size of the training dataset and the presence of a few outliers. Indeed, some finite element simulations
566 produced grains exhibiting von Mises stress values exceeding 3 GPa. These outliers correspond to small grains located at the
567 contact surfaces with the disk. To improve the loss, these outliers could have been removed from the dataset, either by discarding
568 the corresponding graph vertices or by excluding the entire affected graphs. Another possible approach would be to filter the
569 graph nodes based on the grain positions, retaining only those located far from the contact zones. In any case, with the original
570 crystal plasticity law, the von Mises stress remains bounded, as plastic flow develops in this region.

571 The comparison between the predicted grain-averaged von Mises stress and the true one is shown in Figure 13 for the validation
572 and the test dataset. Please note that each figure contains approximately $800,000 = 100 \times 8000$ data points. Transparency
573 is applied to the points to make the data clustering more visible ($\alpha = 0.05$). The red lines represent the perfect prediction, as
574 well as the $\pm 10\%$ and $\pm 20\%$ relative error bounds. As shown in Figure 13, even though the global loss is very low, the error
575 for a given grain can still be significant. However, most points exhibit a relative error below 20%, and the predictions are more
576 accurate for the highly stressed grains than for the weakly loaded ones. This behavior results from the use of the MSE loss. This
577 is intentional, as there is little interest in accurately predicting the response of low-stressed grains.

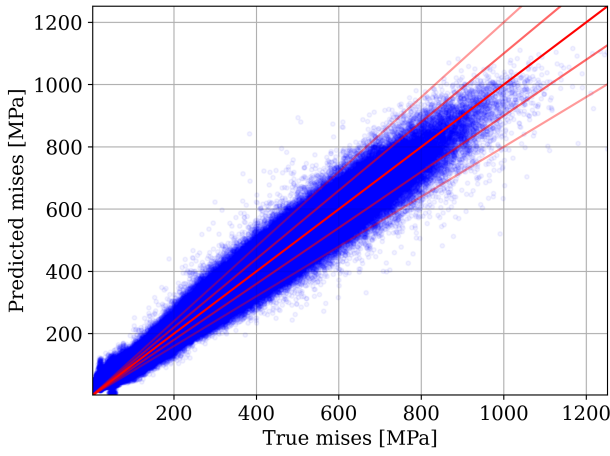
578 6.5.2. Training one GNN for all components

579 This section follows the second strategy, which consists in training a single network to predict all 14 outputs simultaneously:
580 the average values of the stress tensor components and of the von Mises equivalent stress, as well as their spatial standard
581 deviations.

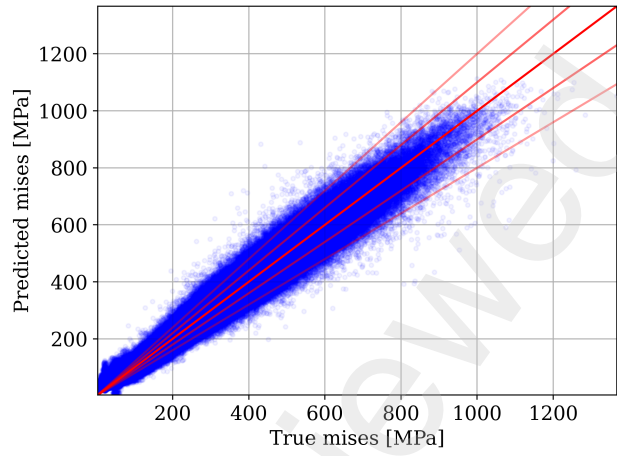
582 *Results obtained with the GraphSAGE architecture.* After 200 epochs, the training loss and the validation loss are 5.31×10^{-5}
583 and 5.49×10^{-5} respectively. The training process takes approximately six hours.

584 The comparison between the predicted grain-averaged von Mises stress and standard deviation and the true ones are shown
585 in Figure 14, only for the test dataset. Figures 15 and 16 provide the same information for the components of the stress tensor.
586 As can be seen by comparing Figures 13 and 14, training one GNN to predict all components yields similar results to training a
587 dedicated GNN.

588 Examining the predictions for the stress tensor components, $\bar{\sigma}_{33}$ is accurately predicted by the GNN. This direction cor-
589 responds to the direction of the centrifugal loading. The $\bar{\sigma}_{11}$ and $\bar{\sigma}_{22}$ are also reasonably well captured. Regarding the shear
590 stresses, the results are more mixed, and no clear trend can be identified. Once again, the use of the MSE loss tends to favor
591 accuracy for values of large-magnitude. The grain-wise standard deviation of the stress components provides insight into the
592 variation of these quantities within each grain. As shown in Figure 16, the GNN performs poorly in predicting small deviations
593 but yields fairly accurate results for larger ones.

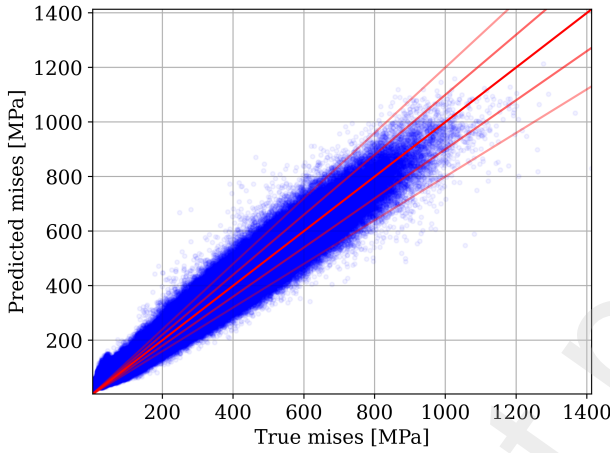


(a) Validation dataset, $\bar{\sigma}_{vm}$.

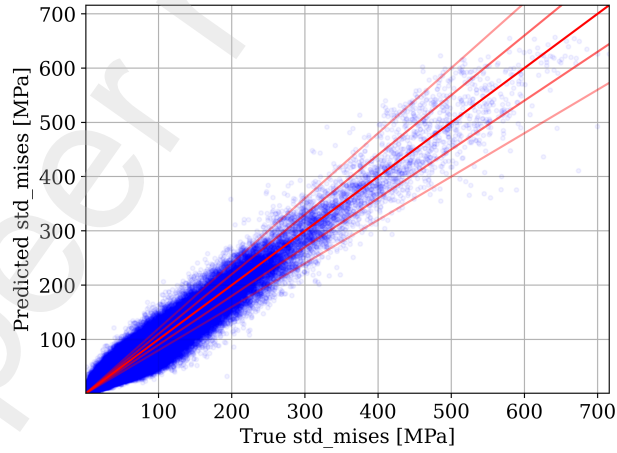


(b) Test dataset, $\bar{\sigma}_{vm}$.

Figure 13: Predicted versus true grain-averaged von Mises stresses for GraphSAGE model (dataset (O)) : the red lines correspond to the perfect prediction, $\pm 10\%$ and $\pm 20\%$ relative errors. One GNN per components.



(a) Test dataset $\bar{\sigma}_{vm}$.



(b) Test dataset $S(\sigma_{vm})$.

Figure 14: Predicted versus true grain-averaged von Mises stress and grain-wise von Mises standard deviation for GraphSAGE model (dataset (O), one GNN for all components).

594 6.6. Regression results for unseen microstructure (dataset (M))

595 For the unseen microstructure dataset (M), both the node features and the edge features vary. Only the first strategy described
596 in section 6.3.1 is applied, that is, training a GNN for each component separately.

597 6.6.1. Results obtained with the GraphSAGE architecture

598 To facilitate training, the model weights were initialized using those obtained from training on dataset (O) (see section 6.5.1),
599 which effectively serves as a pre-training stage. As a result, the initial training loss at the first epoch is already 8.358×10^{-4} .
600 However, as illustrated in Figure 17, the GraphSAGE architecture exhibits difficulty in accurately fitting the data. After 300
601 epochs, the training and validation losses reach 1.707×10^{-4} and 6.207×10^{-4} , respectively. This limitation is not unexpected, as
602 GraphSAGE does not incorporate edge features in its aggregation mechanism. As reported in Figure 17, the comparison between
603 the predicted and true grain-averaged von Mises stresses for the test dataset further illustrates this issue. Notably, without the
604 pre-training step, the optimization process becomes even more challenging.

605 6.6.2. Results obtained with the GENConv architecture

606 The evolution of the loss function and the comparison between the predicted and true von Mises stresses are presented in
607 Figure 18. For GENConv, the initial weights are randomly initialized. The loss evolution is more stable, although a few epochs
608 exhibit noticeable fluctuations. After 400 epochs, the training and validation losses stabilize around 9.2×10^{-5} and 1.2×10^{-4} .
609 The comparison with the ground truth demonstrates a substantially improved agreement with the data. These results highlight
610 the incorporation of edge features is essential for achieving accurate predictions on unseen microstructures. Indeed, GENConv
611 considers the orientation of grain boundaries with respect to mechanical loads and lattice orientations, which is physically sound.

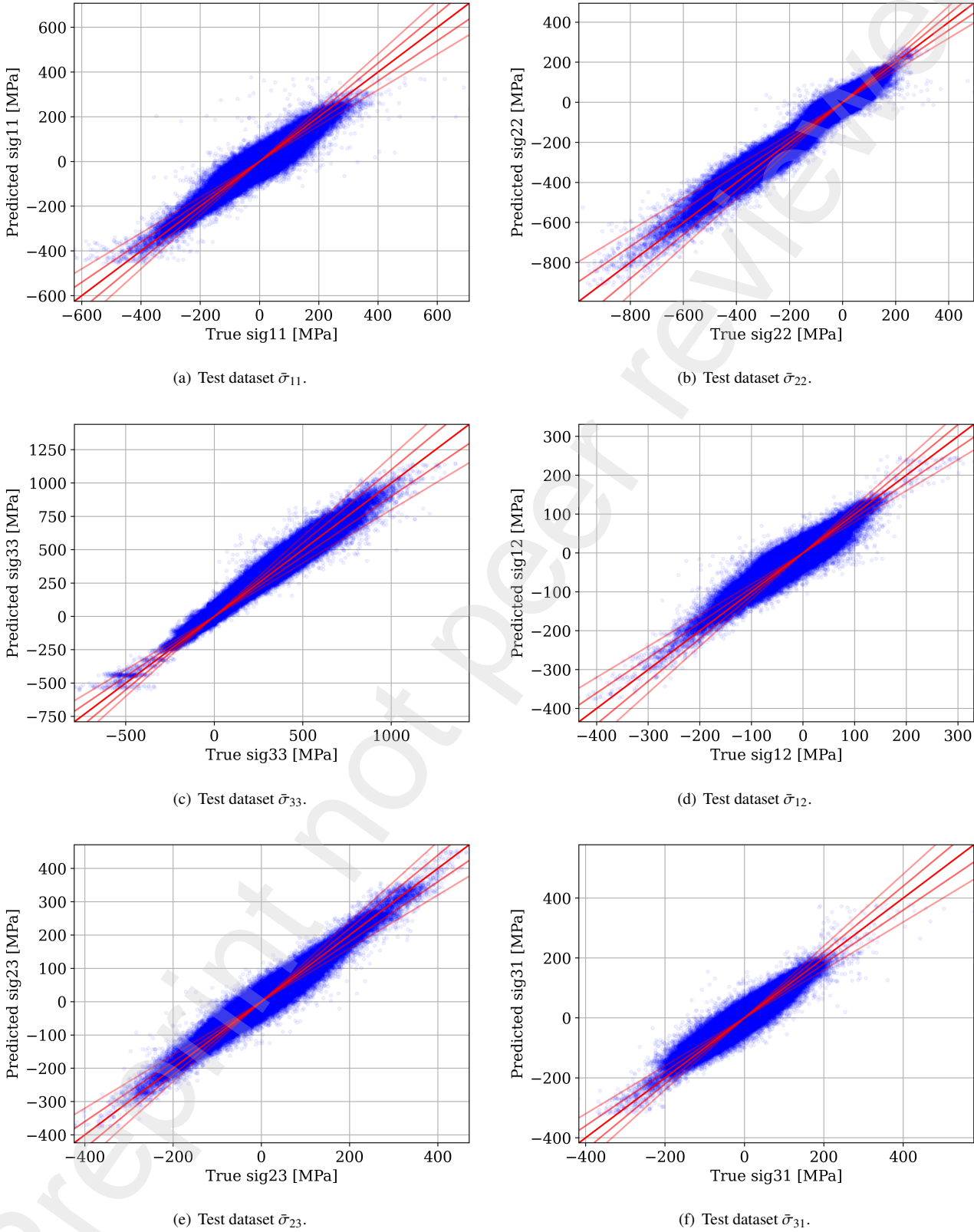
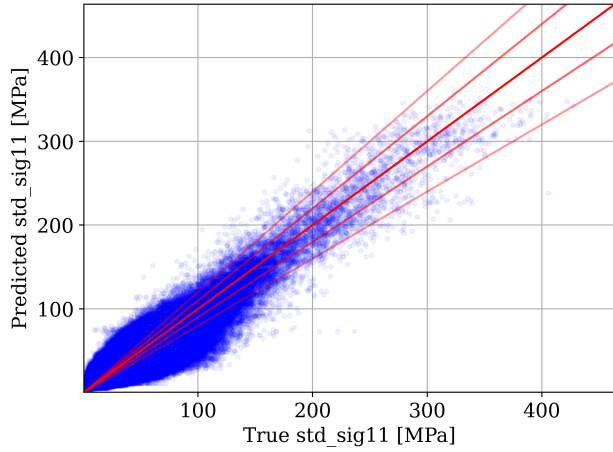
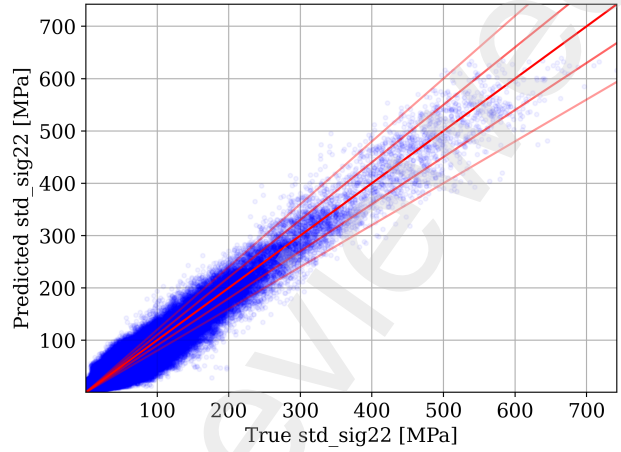


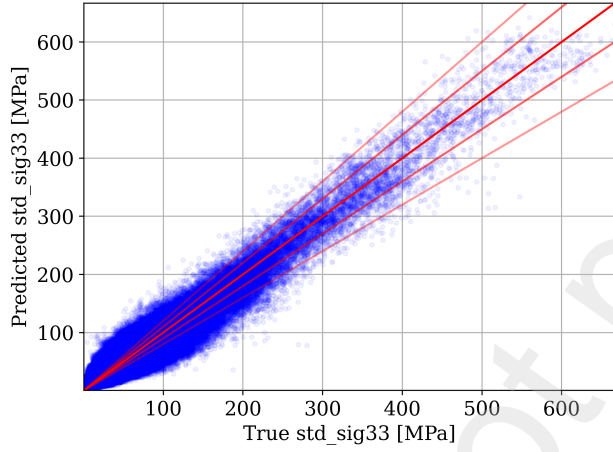
Figure 15: Predicted versus true grain-averaged stress components for GraphSAGE model (dataset (O), one GNN for all components).



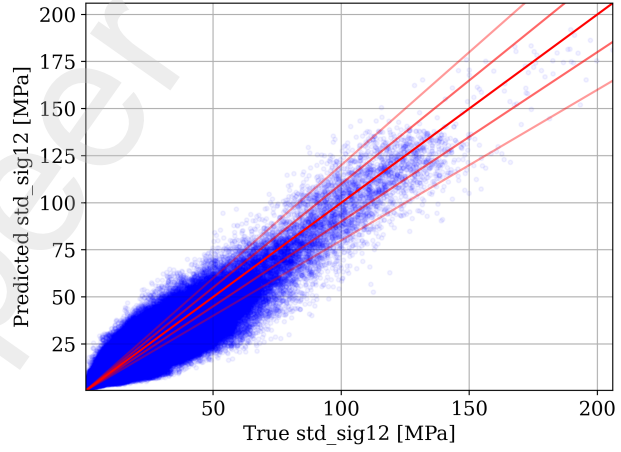
(a) Test dataset $S(\sigma_{11})$.



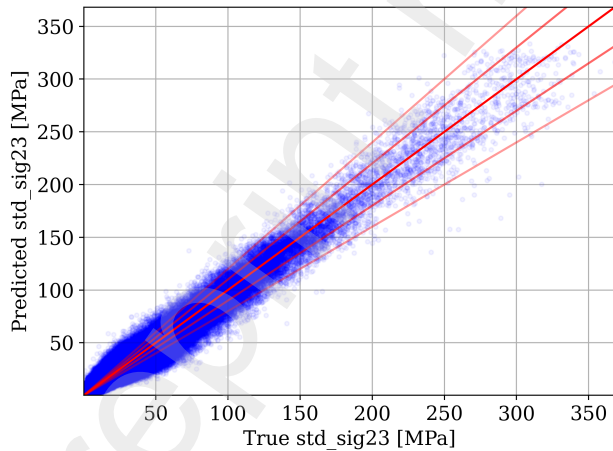
(b) Test dataset $S(\sigma_{22})$.



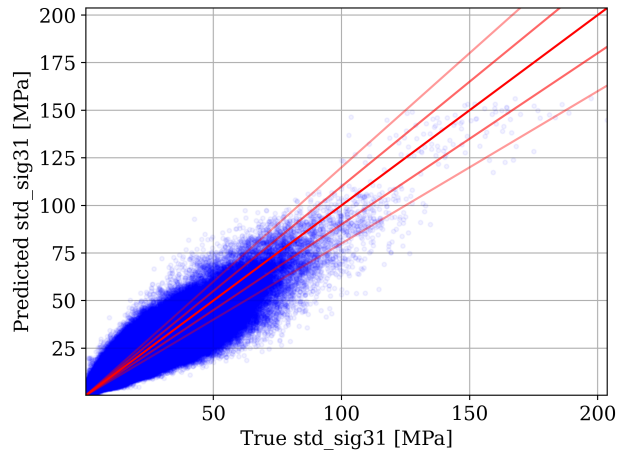
(c) Test dataset $S(\sigma_{33})$.



(d) Test dataset $S(\sigma_{12})$.



(e) Test dataset $S(\sigma_{23})$.



(f) Test dataset $S(\sigma_{31})$.

Figure 16: Predicted versus true grain-wise standard deviation of stress components for GraphSAGE model (dataset (O), one GNN for all components).

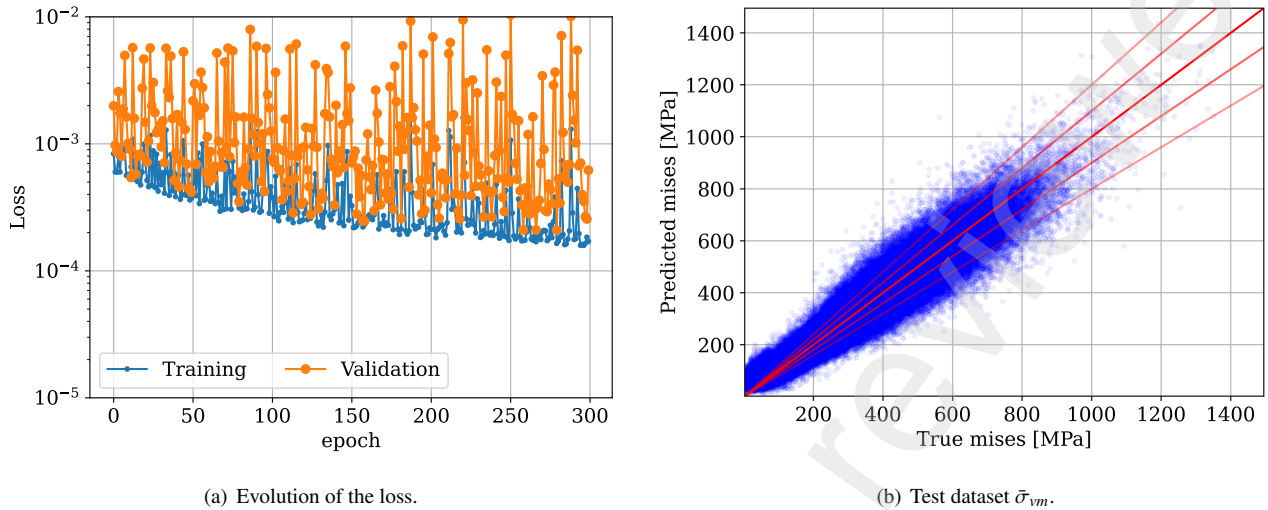


Figure 17: GraphSAGE model (dataset (M)): loss function and predicted versus true grain-averaged von Mises stresses. One GNN per components.

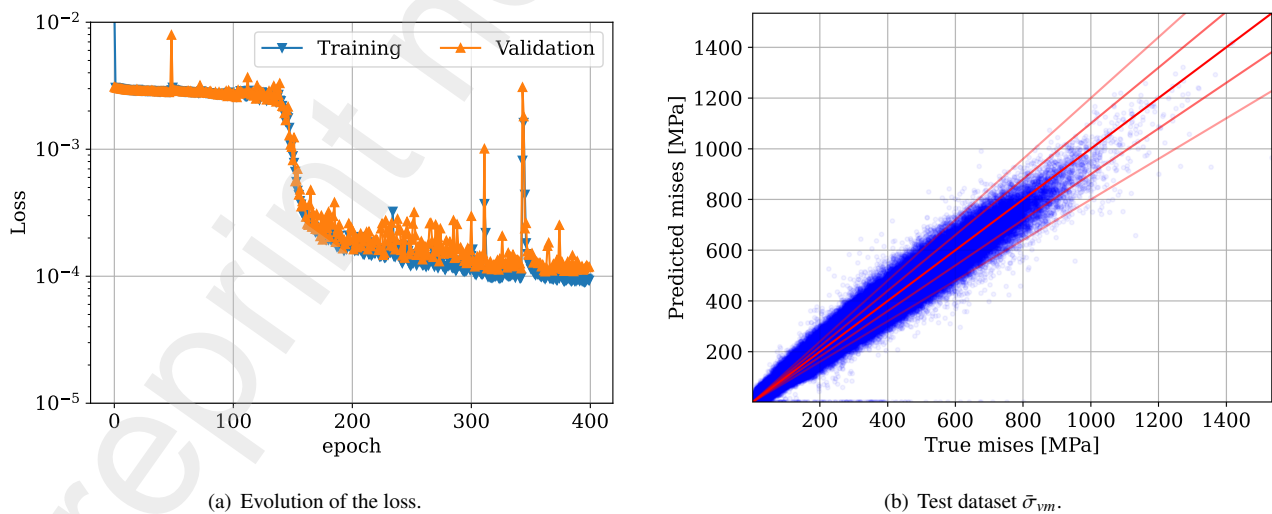


Figure 18: GENConv model (dataset (M)): loss function and predicted versus True grain-averaged von Mises stresses. One GNN per components.

612 7. Conclusion

613 This work introduces a computational framework for full-scale, microstructure-resolved crystal plasticity simulations of poly-
 614 crystalline turbine blades. The framework combines conformal microstructure embedding, a dislocation-density-based crystal
 615 plasticity formulation, and a grain-wise domain decomposition strategy to analyze microstructure-induced mechanical hetero-
 616 geneities at the component scale under realistic thermomechanical loading conditions.

617 A key contribution of this study lies in the robust generation of microstructure-conforming finite element discretizations
 618 for complex industrial geometries. The resulting meshes preserve grain-boundary conformity and geometric fidelity at the
 619 component scale, which is essential to avoid artificial stress concentrations and to enable mechanically meaningful full-field
 620 simulations.

621 The mechanical behavior of Inconel 718 is described using a finite-strain, thermomechanical crystal plasticity model based on
 622 dislocation densities, explicitly accounting for both mobile and geometrically necessary dislocations. This formulation enables
 623 the analysis of lattice curvature, intergranular interactions, and strain localization effects arising from the combined influence of
 624 microstructural heterogeneity and component-level loading paths.

625 The resulting highly nonlinear large-scale problems are efficiently solved using an Adaptive Multipreconditioned FETI do-
 626 main decomposition method combined with a grain-by-grain partitioning strategy. Full-scale simulations involving up to 40,000
 627 grains demonstrate the scalability and robustness of the proposed framework, and allow the systematic analysis of stress localiza-
 628 tion, plastic strain accumulation, grain-size effects, and the interplay between mobile dislocations and GNDs at the component
 629 level.

630 Beyond direct numerical simulation, the generated high-fidelity database provides a valuable basis for reduced-order mod-
 631 eling strategies. In particular, representing blade microstructures as graphs enables the learning of grain-averaged mechanical
 632 responses from morphological and crystallographic descriptors using graph neural networks. While applied to a simplified
 633 version of the constitutive law, these results illustrate the potential of graph-based learning approaches as surrogate models for
 634 microstructure-sensitive mechanical analyses. Two off-the-shelf GNN architectures have been tested, based on Sage and GEN-
 635 Conv convolution layers. Accounting for edge weights, the GENConv architecture outperforms the Sage one when the topology
 636 of the graph changes.

637 Future work will focus on extending the constitutive framework to account for cyclic loading and kinematic hardening
 638 effects relevant to fatigue, as well as on integrating parallel adaptive remeshing strategies to improve robustness under large
 639 deformations. In addition, extending the learning framework to nonlinear crystal plasticity responses and to other classes of
 640 microstructures, such as directionally solidified alloys, appears as a natural continuation of this work.

641 Appendix A. Nonlinear integration

642 At each integration point over the time interval $[t, t + \Delta t]$, the thermal deformation gradient at $t + \Delta t$ is obtained by virtue of
 643 eq. (2) as

$$644 \mathbf{F}_T(t + \Delta t) = (1 + \alpha_T \Delta T) \mathbf{F}_T(t), \quad (\text{A.1})$$

with $\Delta T = \dot{T} \Delta t$, such that

$$\mathbf{F}_T^{-1}(t + \Delta t) = (1 - \alpha_T \Delta T) \mathbf{F}_T^{-1}(t), \quad (\text{A.2})$$

under the assumption of isotropic thermal expansion. The resolved shear stress on the slip system α is given by

$$\tau^\alpha = \det(\mathbf{F}_T) \left(\mathbf{F}_T^t \cdot \mathbf{S} \cdot \mathbf{F}_T^{-t} \right) : \mathbf{m}^\alpha \otimes \mathbf{n}^\alpha, \quad (\text{A.3})$$

since the elastic stretch is negligible for metals.

The plastic deformation gradient is integrated over the increment Δt using the first-order Taylor expansion of the exponential mapping, as follows

$$\mathbf{F}_p(t + \Delta t) = \left(\mathbf{I} + \sum_{\alpha=1}^{12} \Delta \gamma^\alpha \mathbf{m}^\alpha \otimes \mathbf{n}^\alpha \right) \cdot \mathbf{F}_p(t), \quad (\text{A.4})$$

with $\Delta \gamma^\alpha = \dot{\gamma}^\alpha \Delta t$. Thus, the inverse plastic deformation gradient is updated as

$$\mathbf{F}_p^{-1}(t + \Delta t) = \mathbf{F}_p^{-1}(t) \left(\mathbf{I} - \sum_{\alpha=1}^{12} \Delta \gamma^\alpha \mathbf{m}^\alpha \otimes \mathbf{n}^\alpha \right), \quad (\text{A.5})$$

while the elastic deformation gradient is given by

$$\mathbf{F}_e(t + \Delta t) = (1 - \alpha_T \Delta T) \mathbf{F}(t + \Delta t) \cdot \mathbf{F}_T^{-1}(t) \cdot \mathbf{F}_p^{-1}(t) \cdot \left(\mathbf{I} - \sum_{\alpha=1}^{12} \Delta \gamma^\alpha \mathbf{m}^\alpha \otimes \mathbf{n}^\alpha \right), \quad (\text{A.6})$$

so that the elastic Cauchy-Green tensor \mathbf{C}_e is

$$\mathbf{C}_e(t + \Delta t) = (1 - 2\alpha_T \Delta T) \left(\mathbf{C}_\star - \sum_{\alpha=1}^{12} \Delta \gamma^\alpha (\mathbf{C}_\star \cdot \mathbf{m}^\alpha \otimes \mathbf{n}^\alpha + \mathbf{n}^\alpha \otimes \mathbf{m}^\alpha \cdot \mathbf{C}_\star') \right), \quad (\text{A.7})$$

within which the trial elastic right Cauchy-Green tensor \mathbf{C}_\star is

$$\mathbf{C}_\star = \mathbf{F}_e^t(t) \cdot \Delta \mathbf{F}^t \cdot \Delta \mathbf{F} \cdot \mathbf{F}_e(t), \quad (\text{A.8})$$

with $\Delta \mathbf{F} = \mathbf{F}(t + \Delta t) \cdot \mathbf{F}_t^{-1}(t)$ the incremental deformation gradient.

Eq. (A.8) provides a kinematic predictor by pulling back the incremental metric $\Delta \mathbf{F}^T \Delta \mathbf{F}$ to the intermediate configuration, yielding the trial tensor \mathbf{C}_\star . The state at $t + \Delta t$ is then obtained by a local Newton-Raphson solve enforcing the constitutive hardening and plastic flow relations. The unknown vector is $\mathbf{x} \in V = \{\mathbf{E}_e, \{\Delta \gamma^\alpha, \Delta \rho^\alpha\}_{\alpha=1,\dots,12}\}$, and both the residual $\mathbf{R}(\mathbf{x}) = \{r_{\mathbf{E}_e}, r_\gamma, r_\rho\}$ and the consistent Jacobian $\mathbf{J} = \partial \mathbf{R} / \partial \mathbf{x}$ are evaluated at the material-point level.

The residuals are defined by

$$\begin{aligned} r_{\mathbf{E}_e} &= \mathbf{E}_e(t + \Delta t) - \frac{1}{2} \exp(-2\alpha_T \Delta T) \mathbf{C}_\star + \exp(-2\alpha_T \Delta T) \sum_{\alpha=1}^{12} \Delta \gamma^\alpha \mathbf{P}^\alpha + \frac{1}{2} \mathbf{I}, \\ r_\gamma &= \Delta \gamma^\alpha - \dot{\gamma}^\alpha \Delta t = \Delta \gamma^\alpha - \rho^\alpha b^\alpha v^\alpha \operatorname{sign}(\tau^\alpha) \Delta t, \\ r_\rho &= \Delta \rho^\alpha - \frac{1}{b^\alpha} \left(\frac{1}{K} \sqrt{\sum_{\beta=1}^{12} h^{\alpha\beta} \rho^\beta} - 2y_c \rho^\alpha \right) \Delta \gamma^\alpha \operatorname{sign}(\tau^\alpha), \end{aligned} \quad (\text{A.9})$$

according to eqs. (3), (9) and (A.7), while the symmetrical tensor \mathbf{P}^α is defined by

$$\mathbf{P}^\alpha = \frac{1}{2} (\mathbf{C}_\star \cdot \mathbf{m}^\alpha \otimes \mathbf{n}^\alpha + \mathbf{n}^\alpha \otimes \mathbf{m}^\alpha \cdot \mathbf{C}_\star^t), \quad (\text{A.10})$$

so that the corresponding Jacobian matrix \mathbf{J} is locally defined by

$$\begin{aligned} \mathbf{J} &= \begin{bmatrix} \frac{\partial r_E}{\partial \mathbf{E}_e} & \frac{\partial r_E}{\partial \Delta \gamma^\alpha} & \frac{\partial r_E}{\partial \Delta \rho^\alpha} \\ \frac{\partial r_\gamma}{\partial \mathbf{E}_e} & \frac{\partial r_\gamma}{\partial \Delta \gamma^\alpha} & \frac{\partial r_\gamma}{\partial \Delta \rho^\alpha} \\ \frac{\partial r_\rho}{\partial \mathbf{E}_e} & \frac{\partial r_\rho}{\partial \Delta \gamma^\alpha} & \frac{\partial r_\rho}{\partial \Delta \rho^\alpha} \end{bmatrix} \\ &= \begin{bmatrix} \mathbb{I} + \exp(-2\alpha_T \Delta T) \sum_{\alpha=1}^{12} \mathbf{P}^\alpha \otimes \frac{\partial \dot{\gamma}^\alpha}{\partial \tau^\alpha} \frac{\partial \tau^\alpha}{\partial \mathbf{E}_e} \Delta t & \exp(-2\alpha_T \Delta T) \mathbf{P}^\alpha & 0 \\ \frac{\partial r_\gamma}{\partial \tau^\alpha} \frac{\partial \tau^\alpha}{\partial \mathbf{E}_e} & \delta_{\alpha\beta} & \frac{\partial r_\gamma}{\partial \tau_A^\alpha} \frac{\partial \tau_A^\alpha}{\partial \Delta \rho^\beta} \\ 0 & \frac{\partial r_\rho}{\partial \Delta \gamma^\beta} & \frac{\partial r_\rho}{\partial \Delta \rho^\beta} \end{bmatrix}, \end{aligned} \quad (\text{A.11})$$

where the remaining partial derivatives with respect to the unknowns are given in closed form as follows

$$\frac{\partial \dot{\gamma}^\alpha}{\partial \tau^\alpha} = \rho^\alpha b^\alpha \frac{\partial v^\alpha}{\partial \tau^\alpha} \operatorname{sign}(\tau^\alpha), \quad (\text{A.12})$$

$$\frac{\partial v^\alpha}{\partial \tau^\alpha} = \frac{2v_D l^\alpha b^{\alpha 2} \left(l_L^{\alpha 2} \exp\left(\frac{Q_s^\alpha}{k_B T}\right) \cosh\left(\frac{|\tau^\alpha| - \tau_A^\alpha}{\tau_T^\alpha}\right) (|\tau^\alpha| - \tau_A^\alpha)^2 + B_0 v_D l^\alpha b^\alpha \tau_T^\alpha \left(\cosh\left(2\frac{|\tau^\alpha| - \tau_A^\alpha}{\tau_T^\alpha}\right) - 1 \right) \right)}{\tau_T^\alpha \left(2B_0 v_D l^\alpha b^\alpha \sinh\left(\frac{|\tau^\alpha| - \tau_A^\alpha}{\tau_T^\alpha}\right) + l_L^{\alpha 2} \exp\left(\frac{Q_s^\alpha}{k_B T}\right) (|\tau^\alpha| - \tau_A^\alpha) \right)^2}, \quad (\text{A.13})$$

$$\frac{\partial \tau^\alpha}{\partial \mathbf{E}_e} = \det(\mathbf{F}_T) \mathbb{C} : \mathbf{m}^\alpha \otimes \mathbf{n}^\alpha, \quad (\text{A.14})$$

$$\frac{\partial r_\gamma}{\partial \tau^\alpha} = -\frac{\partial \dot{\gamma}^\alpha}{\partial \tau^\alpha} \Delta t, \quad (\text{A.15})$$

$$\frac{\partial r_\gamma}{\partial \tau_A^\alpha} = -\frac{\partial r_\gamma}{\partial \tau^\alpha}, \quad (\text{A.16})$$

$$\frac{\partial \tau_A^\alpha}{\partial \Delta \rho^\beta} = \frac{\alpha_A \mu b^\alpha h^{\alpha\beta}}{2 \sqrt{\sum_{\zeta=1}^{12} h^{\alpha\zeta} \rho^\zeta}}, \quad (\text{A.17})$$

$$\frac{\partial r_{\rho^\alpha}}{\partial \Delta \gamma^\beta} = -\frac{1}{b^\alpha} \left(\frac{1}{K} \sqrt{\sum_{\zeta=1}^{12} h^{\alpha\zeta} \rho^\zeta} - 2y_c \rho^\alpha \right) \delta_{\alpha\beta} \operatorname{sign}(\tau^\alpha), \quad (\text{A.18})$$

$$\frac{\partial r_{\rho^\alpha}}{\partial \Delta \rho^\beta} = \left(1 + \frac{2y_c \Delta \gamma^\alpha \operatorname{sign}(\tau^\alpha)}{b^\alpha} \right) \delta_{\alpha\beta} - \frac{1}{2Kb^\alpha} \frac{1}{\sqrt{\sum_{\zeta=1}^{12} h^{\alpha\zeta} \rho^\zeta}} \Delta \gamma^\alpha h^{\alpha\beta} \operatorname{sign}(\tau^\alpha), \quad (\text{A.19})$$

662 with $\det(F_T) = \exp(3\alpha_T \Delta T)$.

663 Acknowledgements

664 This work was supported by the French Civil Aviation Authority (DGAC), by the France Relance program, and by the
665 European Union through the NextGenerationEU initiative (grant no. 2021-08, ARIZE project).

666 Data availability

667 The data supporting the findings of this study are available from the corresponding author upon reasonable request. The
668 initial turbine blade geometry used in this work is publicly available online, as indicated in the manuscript.

669 Declaration of generative AI and AI-assisted technologies in the writing process

670 During the preparation of this manuscript, the authors used ChatGPT (OpenAI, 2025) to improve the clarity, style, and
671 grammar of the English text, as the authors are not native English speakers. After using this tool, the authors carefully reviewed
672 and edited the content as needed and take full responsibility for the content of the published article.

673 References

- 674 Alankar, A., Eisenlohr, P., Raabe, D., 2011. A dislocation density-based crystal plasticity constitutive model for prismatic
675 slip in α -titanium. *Acta Materialia* 59, 7003–7009. URL: <https://www.sciencedirect.com/science/article/pii/S1359645411005398>, doi:<https://doi.org/10.1016/j.actamat.2011.07.053>.
- 677 Amadou Sanoko, A.M., Essongue, S., Gélébart, L., Lapostolle, L., Morin, L., Paux, J., 2025. A FFT-based numerical scheme for
678 the transient conductivity of heterogeneous materials with non-periodic boundary conditions. *European Journal of Mechanics - A/Solids* 113, 105680. URL: <https://www.sciencedirect.com/science/article/pii/S0997753825001147>,
680 doi:[10.1016/j.euromechsol.2025.105680](https://doi.org/10.1016/j.euromechsol.2025.105680).
- 681 Ardeljan, M., Beyerlein, I.J., Knezevic, M., 2017. Effect of dislocation density-twin interactions on twin growth in az31
682 as revealed by explicit crystal plasticity finite element modeling. *International Journal of Plasticity* 99, 81–101. URL:
683 <https://www.sciencedirect.com/science/article/pii/S0749641917302553>, doi:<https://doi.org/10.1016/j.ijplas.2017.09.002>.
- 685 Arsenlis, A., Parks, D., 1999. Crystallographic aspects of geometrically-necessary and statistically-stored disloca-
686 tion density. *Acta Materialia* 47, 1597–1611. URL: <https://www.sciencedirect.com/science/article/pii/S1359645499000208>, doi:[https://doi.org/10.1016/S1359-6454\(99\)00020-8](https://doi.org/10.1016/S1359-6454(99)00020-8).
- 688 Asaro, R., Rice, J., 1977. Strain localization in ductile single crystals. *Journal of the Mechanics and Physics of Solids* 25,
689 309–338. URL: <https://www.sciencedirect.com/science/article/pii/0022509677900011>, doi:[https://doi.org/10.1016/0022-5096\(77\)90001-1](https://doi.org/10.1016/0022-5096(77)90001-1).
- 691 Austin, R.A., McDowell, D.L., 2011. A dislocation-based constitutive model for viscoplastic deformation of fcc metals at
692 very high strain rates. *International Journal of Plasticity* 27, 1–24. URL: <https://www.sciencedirect.com/science/article/pii/S0749641910000380>, doi:<https://doi.org/10.1016/j.ijplas.2010.03.002>.
- 694 Bovet, C., 2022. On the use of graph centralities to compute generalized inverse of singular finite element operators: Applications
695 to the analysis of floating substructures. *International Journal for Numerical Methods in Engineering* 124, 1933–1964. doi:[10.1002/nme.7193](https://doi.org/10.1002/nme.7193).

- 697 Bovet, C., Parret-Fréaud, A., Gosselet, P., 2021. Two-level adaptation for Adaptive Multipreconditioned FETI. Advances in
698 Engineering Software 152, 102952. URL: <https://hal.science/hal-03081712>, doi:10.1016/j.advengsoft.2020.
699 102952.
- 700 Bovet, C., Parret-Fréaud, A., Spillane, N., Gosselet, P., 2017. Adaptive multipreconditioned FETI: Scalability results and
701 robustness assessment. Computers & Structures , 1–20doi:10.1016/j.compstruc.2017.07.010.
- 702 Cailletaud, G., Forest, S., Jeulin, D., Feyel, F., Galliet, I., Mounoury, V., Quilici, S., 2003. Some elements of microstructural me-
703 chanics. Computational Materials Science 27, 351–374. URL: <https://www.sciencedirect.com/science/article/pii/S0927025603000417>, doi:10.1016/S0927-0256(03)00041-7.
- 705 Charpagne, M., Hestroffer, J., Polonsky, A., Echlin, M., Texier, D., Valle, V., Beyerlein, I., Pollock, T., Stinville, J., 2021.
706 Slip localization in inconel 718: A three-dimensional and statistical perspective. Acta Materialia 215, 117037. URL:
707 <https://www.sciencedirect.com/science/article/pii/S1359645421004171>, doi:<https://doi.org/10.1016/j.actamat.2021.117037>.
- 709 Chen, Y., Vasiukov, D., Gélébart, L., Park, C.H., 2019. A fft solver for variational phase-field modeling of brittle fracture.
710 Computer Methods in Applied Mechanics and Engineering 349, 167–190. URL: <https://www.sciencedirect.com/science/article/pii/S004578251930088X>, doi:<https://doi.org/10.1016/j.cma.2019.02.017>.
- 712 Chen, Z., Tan, T.S., 2019. Computing Three-Dimensional Constrained Delaunay Refinement Using the GPU, in: 2019 28th
713 International Conference on Parallel Architectures and Compilation Techniques (PACT), IEEE, Seattle, WA, USA. pp. 409–
714 420. URL: <https://ieeexplore.ieee.org/document/8891648/>, doi:10.1109/PACT.2019.00039.
- 715 Cherchi, G., Pellacini, F., Attene, M., Livesu, M., 2022. Interactive and Robust Mesh Booleans. ACM Transactions on Graphics
716 41, 1–14. URL: <https://dl.acm.org/doi/10.1145/3550454.3555460>, doi:10.1145/3550454.3555460.
- 717 Cormier, J., Cailletaud, G., 2010. Constitutive modeling of the creep behavior of single crystal superalloys under non-
718 isothermal conditions inducing phase transformations. Materials Science and Engineering: A 527, 6300–6312. URL:
719 <https://www.sciencedirect.com/science/article/pii/S0921509310006568>, doi:<https://doi.org/10.1016/j.msea.2010.06.023>.
- 721 Coudon, F., Gourdin, S., Boucicaud, A., Rose, T., Cailletaud, G., 2020. A stochastic approach applied to directionally solidified
722 turbine blades. International Journal of Solids and Structures 184, 193–201. URL: <https://www.sciencedirect.com/science/article/pii/S0020768319301763>, doi:10.1016/j.ijsolstr.2019.04.007.
- 724 Dapogny, C., Dobrzynski, C., Frey, P., 2014. Three-dimensional adaptive domain remeshing, implicit domain meshing, and
725 applications to free and moving boundary problems. Journal of Computational Physics 262, 358–378. URL: <https://linkinghub.elsevier.com/retrieve/pii/S0021999114000266>, doi:10.1016/j.jcp.2014.01.005.
- 727 Demir, E., Horton, E.W., Kareer, A., Collins, D.M., Mostafavi, M., Knowles, D., 2023. A finite element method to calculate
728 geometrically necessary dislocation density: Accounting for orientation discontinuities in polycrystals. Acta Materialia 245,
729 118658. URL: <https://www.sciencedirect.com/science/article/pii/S1359645422010333>, doi:<https://doi.org/10.1016/j.actamat.2022.118658>.
- 731 Desmorat, R., Mattiello, A., Cormier, J., 2017. A tensorial thermodynamic framework to account for the γ' rafting in nickel-
732 based single crystal superalloys. International Journal of Plasticity 95, 43–81. URL: <https://www.sciencedirect.com/science/article/pii/S0921509310006568>, doi:<https://doi.org/10.1016/j.ijplas.2017.03.010>.
- 734 Ehab Moustafa Kamel, K., Sonon, B., Massart, T.J., 2019. An integrated approach for the conformal discretization of complex
735 inclusion-based microstructures. Computational Mechanics 64, 1049–1071. URL: <http://link.springer.com/10.1007/s00466-019-01693-4>, doi:10.1007/s00466-019-01693-4.
- 737 Ekkehart, K., 1958. Kontinuumstheorie der Versetzungen und Eigenspannungen. Springer Berlin Heidelberg. URL: <https://cir.nii.ac.jp/crid/1364233270957915392>, doi:10.1007/978-3-642-94719-3.
- 739 Farhat, C., Roux, F.X., 1991. A method of finite element tearing and interconnecting and its parallel solution algorithm. International Journal for Numerical Methods in Engineering 32, 1205. doi:10.1002/nme.1620320604.
- 741 Fedelich, B., 1999. A microstructure based constitutive model for the mechanical behavior at high temperatures of nickel-
742 base single crystal superalloys. Computational Materials Science 16, 248–258. URL: <https://www.sciencedirect.com/science/article/pii/S0927025699000671>, doi:[https://doi.org/10.1016/S0927-0256\(99\)00067-1](https://doi.org/10.1016/S0927-0256(99)00067-1).
- 744 Frankel, A.L., Safta, C., Alleman, C., Jones, R., 2022. MESH-BASED GRAPH CONVOLUTIONAL NEURAL NETWORKS FOR
745 MODELING MATERIALS WITH MICROSTRUCTURE. Journal of Machine Learning for Modeling and
746 Computing 3, 1–30. URL: <http://www.dl.begellhouse.com/journals/558048804a15188a,441149b76421ea9,22a9a07f1f04b5a7.html>, doi:10.1615/JMachLearnModelComput.2021039688.

- 748 Frutschy, K., Clifton, R., 1998. High-temperature pressure-shear plate impact experiments on ofhc copper. Journal of the
749 Mechanics and Physics of Solids 46, 1723–1744. URL: <https://www.sciencedirect.com/science/article/pii/S0022509698000556>, doi:[https://doi.org/10.1016/S0022-5096\(98\)00055-6](https://doi.org/10.1016/S0022-5096(98)00055-6).
- 750
- 751 Frydrych, K., Kowalczyk-Gajewska, K., Prakash, A., 2019. On solution mapping and remeshing in crystal plasticity finite
752 element simulations: application to equal channel angular pressing. Modelling and Simulation in Materials Science and
753 Engineering 27, 075001. URL: <https://doi.org/10.1088/1361-651X/ab28e3>, doi:[10.1088/1361-651X/ab28e3](https://doi.org/10.1088/1361-651X/ab28e3). publisher: IOP Publishing.
- 754
- 755 Gao, Z., Zhu, C., Wang, C., Shu, Y., Liu, S., Miao, J., Yang, L., 2025. Advanced deep learning framework for multi-
756 scale prediction of mechanical properties from microstructural features in polycrystalline materials. Computer Methods in
757 Applied Mechanics and Engineering 438, 117844. URL: <https://www.sciencedirect.com/science/article/pii/S0045782525001161>, doi:[10.1016/j.cma.2025.117844](https://doi.org/10.1016/j.cma.2025.117844).
- 758
- 759 Gierden, C., Kochmann, J., Waimann, J., Svendsen, B., Reese, S., 2022. A review of fe-fft-based two-scale meth-
760 ods for computational modeling of microstructure evolution and macroscopic material behavior. Archives of Compu-
761 tational Methods in Engineering 29, 4115–4135. URL: <https://doi.org/10.1007/s11831-022-09735-6>, doi:[10.1007/s11831-022-09735-6](https://doi.org/10.1007/s11831-022-09735-6).
- 762
- 763 Gosselet, P., Rixen, D., Roux, F.X., Spillane, N., 2015. Simultaneous FETI and block FETI: Robust domain decomposition with
764 multiple search directions. International Journal for Numerical Methods in Engineering 104, 905–927. doi:[10.1002/nme.4946](https://doi.org/10.1002/nme.4946).
- 765
- 766 Groeber, M.A., Jackson, M.A., 2014. DREAM.3D: A Digital Representation Environment for the Analysis of Microstructure
767 in 3D. Integrating Materials and Manufacturing Innovation 3, 56–72. URL: <https://link.springer.com/10.1186/2193-9772-3-5>, doi:[10.1186/2193-9772-3-5](https://doi.org/10.1186/2193-9772-3-5).
- 768
- 769 Guo, J.P., Fu, X.M., 2024. Exact and Efficient Intersection Resolution for Mesh Arrangements. ACM Transactions on Graphics
770 43, 1–14. URL: <https://dl.acm.org/doi/10.1145/3687925>, doi:[10.1145/3687925](https://doi.org/10.1145/3687925).
- 771
- 772 Hamilton, W.L., Ying, R., Leskovec, J., 2018. Inductive Representation Learning on Large Graphs. URL: <http://arxiv.org/abs/1706.02216>, doi:[10.48550/arXiv.1706.02216](https://doi.org/10.48550/arXiv.1706.02216). arXiv:1706.02216 [cs].
- 773
- 774 Hestroffer, J.M., Charpagne, M.A., Latypov, M.I., Beyerlein, I.J., 2023. Graph neural networks for efficient learning of mechan-
775 ical properties of polycrystals. Computational Materials Science 217, 111894. URL: <https://www.sciencedirect.com/science/article/pii/S092702562200605X>, doi:[10.1016/j.commatsci.2022.111894](https://doi.org/10.1016/j.commatsci.2022.111894).
- 776
- 777 Hiratani, M., Zbib, H., Khaleel, M., 2003. Modeling of thermally activated dislocation glide and plastic flow through local ob-
778 stacles. International Journal of Plasticity 19, 1271–1296. URL: <https://www.sciencedirect.com/science/article/pii/S0749641902000165>, doi:[https://doi.org/10.1016/S0749-6419\(02\)00016-5](https://doi.org/10.1016/S0749-6419(02)00016-5).
- 779
- 780 Hou, J., Wicks, B.J., Antoniou, R.A., 2002. An investigation of fatigue failures of turbine blades in a gas turbine engine
781 by mechanical analysis. Engineering Failure Analysis 9, 201–211. URL: <https://www.sciencedirect.com/science/article/pii/S135063070100005X>, doi:[https://doi.org/10.1016/S1350-6307\(01\)00005-X](https://doi.org/10.1016/S1350-6307(01)00005-X).
- 782
- 783 Kocks, U., Mecking, H., 2003. Physics and phenomenology of strain hardening: the fcc case. Progress in Materials Science 48,
784 171–273. URL: <https://www.sciencedirect.com/science/article/pii/S0079642502000038>, doi:[https://doi.org/10.1016/S0079-6425\(02\)00003-8](https://doi.org/10.1016/S0079-6425(02)00003-8).
- 785
- 786 Lebensohn, R.A., Kanjrala, A.K., Eisenlohr, P., 2012. An elasto-viscoplastic formulation based on fast Fourier transforms
787 for the prediction of micromechanical fields in polycrystalline materials. International Journal of Plasticity 32–33, 59–
788 69. URL: <https://www.sciencedirect.com/science/article/pii/S0749641911001951>, doi:[10.1016/j.ijplas.2011.12.005](https://doi.org/10.1016/j.ijplas.2011.12.005).
- 789
- 790 Lee, S.B., Lebensohn, R.A., Rollett, A.D., 2011. Modeling the viscoplastic micromechanical response of two-phase materials
791 using Fast Fourier Transforms. International Journal of Plasticity 27, 707–727. URL: <https://www.sciencedirect.com/science/article/pii/S0749641910001270>, doi:[10.1016/j.ijplas.2010.09.002](https://doi.org/10.1016/j.ijplas.2010.09.002).
- 792
- 793 Li, G., Xiong, C., Thabet, A., Ghanem, B., 2020. DeeperGCN: All You Need to Train Deeper GCNs URL: <http://arxiv.org/abs/2006.07739>, doi:[10.48550/arXiv.2006.07739](https://doi.org/10.48550/arXiv.2006.07739). arXiv:2006.07739 [cs].
- 794
- 795 Lévy, B., 2025. Exact predicates, exact constructions and combinatorics for mesh CSG. URL: <http://arxiv.org/abs/2405.12949>, doi:[10.48550/arXiv.2405.12949](https://doi.org/10.48550/arXiv.2405.12949). arXiv:2405.12949 [cs].
- 796
- 797 Ma, A., Roters, F., Raabe, D., 2006. A dislocation density based constitutive model for crystal plasticity fem including geo-
798 metricaly necessary dislocations. Acta Materialia 54, 2169–2179. URL: <https://www.sciencedirect.com/science/article/pii/S1359645406000747>, doi:<https://doi.org/10.1016/j.actamat.2006.01.005>.
- 798

- 799 Meissonnier, F., Busso, E., O'Dowd, N., 2001. Finite element implementation of a generalised non-local rate-
800 dependent crystallographic formulation for finite strains. International Journal of Plasticity 17, 601–640. URL:
801 <https://www.sciencedirect.com/science/article/pii/S0749641900000644>, doi:[https://doi.org/10.1016/S0749-6419\(00\)00064-4](https://doi.org/10.1016/S0749-6419(00)00064-4).
- 803 Nye, J., 1953. Some geometrical relations in dislocated crystals. Acta Metallurgica 1, 153–162. URL: <https://www.sciencedirect.com/science/article/pii/0001616053900546>, doi:[https://doi.org/10.1016/0001-6160\(53\)90054-6](https://doi.org/10.1016/0001-6160(53)90054-6).
- 806 OpenAI, 2025. Chatgpt. <https://chat.openai.com/>. Large language model used to assist with English language editing.
- 807 Quey, R., Dawson, P., Barbe, F., 2011. Large-scale 3D random polycrystals for the finite element method: Generation, meshing
808 and remeshing. Computer Methods in Applied Mechanics and Engineering 200, 1729–1745. URL: <https://linkinghub.elsevier.com/retrieve/pii/S004578251100003X>, doi:[10.1016/j.cma.2011.01.002](https://doi.org/10.1016/j.cma.2011.01.002).
- 810 Ren, S.C., Morgeneyer, T.F., Mazière, M., Forest, S., Rousselier, G., 2019. Portevin-le chatelier effect triggered by complex
811 loading paths in an al-cu aluminium alloy. Philosophical Magazine 99, 659–678. URL: <https://doi.org/10.1080/14786435.2018.1550296>, doi:[10.1080/14786435.2018.1550296](https://doi.org/10.1080/14786435.2018.1550296).
- 813 Resk, H., Delannay, L., Bernacki, M., Coupez, T., Logé, R., 2009. Adaptive mesh refinement and automatic remeshing in crystal
814 plasticity finite element simulations. Modelling and Simulation in Materials Science and Engineering 17, 075012. URL:
815 <https://doi.org/10.1088/0965-0393/17/7/075012>, doi:[10.1088/0965-0393/17/7/075012](https://doi.org/10.1088/0965-0393/17/7/075012).
- 816 Rixen, D.J., Farhat, C., 1999. A simple and efficient extension of a class of substructure based preconditioners to heterogeneous
817 structural mechanics problems. International Journal for Numerical Methods in Engineering 44, 489–516. doi:[10.1002/\(SICI\)1097-0207\(19990210\)44:4<489::AID-NME514>3.0.CO;2-Z](https://doi.org/10.1002/(SICI)1097-0207(19990210)44:4<489::AID-NME514>3.0.CO;2-Z).
- 819 Roters, F., Diehl, M., Shanthraj, P., Eisenlohr, P., Reuber, C., Wong, S., Maiti, T., Ebrahimi, A., Hochrainer, T., Fabritius,
820 H.O., Nikolov, S., Friák, M., Fujita, N., Grilli, N., Janssens, K., Jia, N., Kok, P., Ma, D., Meier, F., Werner, E., Stricker,
821 M., Weygand, D., Raabe, D., 2019. DAMASK – The Düsseldorf Advanced Material Simulation Kit for modeling multi-
822 physics crystal plasticity, thermal, and damage phenomena from the single crystal up to the component scale. Computational
823 Materials Science 158, 420–478. URL: <https://linkinghub.elsevier.com/retrieve/pii/S0927025618302714>,
824 doi:[10.1016/j.commatsci.2018.04.030](https://doi.org/10.1016/j.commatsci.2018.04.030).
- 825 Shahba, A., Ghosh, S., 2016. Crystal plasticity fe modeling of ti alloys for a range of strain-rates. part i: A unified constitutive
826 model and flow rule. International Journal of Plasticity 87, 48–68. URL: <https://www.sciencedirect.com/science/article/pii/S074964191630153X>, doi:<https://doi.org/10.1016/j.ijplas.2016.09.002>.
- 828 Si, H., 2015. TetGen, a Delaunay-Based Quality Tetrahedral Mesh Generator. ACM Transactions on Mathematical Software 41,
829 1–36. URL: <https://dl.acm.org/doi/10.1145/2629697>, doi:[10.1145/2629697](https://doi.org/10.1145/2629697).
- 830 Skamniotis, C., Grilli, N., Cocks, A.C.F., 2023. Crystal plasticity analysis of fatigue-creep behavior at cooling holes in single
831 crystal Nickel based gas turbine blade components. International Journal of Plasticity 166, 103589. URL: <https://www.sciencedirect.com/science/article/pii/S074964192300075X>, doi:[10.1016/j.ijplas.2023.103589](https://doi.org/10.1016/j.ijplas.2023.103589).
- 833 Spillane, N., 2016. An Adaptive Multipreconditioned Conjugate Gradient Algorithm. SIAM J. Sci. Comput. 38, A1896–A1918.
834 doi:[10.1137/15M1028534](https://doi.org/10.1137/15M1028534).
- 835 Tabourot, L., Fivel, M., Rauch, E., 1997. Generalised constitutive laws for f.c.c. single crystals. Materials Science and Engineering: A 234–236, 639–642. URL: <https://www.sciencedirect.com/science/article/pii/S0921509397003535>,
836 doi:[https://doi.org/10.1016/S0921-5093\(97\)00353-5](https://doi.org/10.1016/S0921-5093(97)00353-5).
- 838 Tang, M., Kubin, L., Canova, G., 1998. Dislocation mobility and the mechanical response of b.c.c. single crystals: A meso-
839scopic approach. Acta Materialia 46, 3221–3235. URL: <https://www.sciencedirect.com/science/article/pii/S1359645498000068>, doi:[https://doi.org/10.1016/S1359-6454\(98\)00006-8](https://doi.org/10.1016/S1359-6454(98)00006-8).
- 841 Vattré, A., Chiaruttini, V., 2022. Singularity-free theory and adaptive finite element computations of arbitrarily-shaped dis-
842 location loop dynamics in 3d heterogeneous material structures. Journal of the Mechanics and Physics of Solids 167,
843 104954. URL: <https://www.sciencedirect.com/science/article/pii/S0022509622001491>, doi:<https://doi.org/10.1016/j.jmps.2022.104954>.
- 845 Vattré, A., Devincre, B., Feyel, F., Gatti, R., Groh, S., Jamond, O., Roos, A., 2014. Modelling crystal plasticity
846 by 3d dislocation dynamics and the finite element method: The discrete-continuous model revisited. Journal of the
847 Mechanics and Physics of Solids 63, 491–505. URL: <https://www.sciencedirect.com/science/article/pii/S0022509613001245>, doi:<https://doi.org/10.1016/j.jmps.2013.07.003>.
- 849 Vattré, A., Fedelich, B., 2011. On the relationship between anisotropic yield strength and internal stresses in single crystal
850 superalloys. Mechanics of Materials 43, 930–951. URL: <https://www.sciencedirect.com/science/article/pii/S0167663611001244>, doi:<https://doi.org/10.1016/j.mechmat.2011.07.007>.

- 852 Yan, B., Jiang, S., Hu, L., Zhang, Y., Sun, D., 2021. Crystal plasticity finite element simulation of niti shape mem-
853 ory alloy under canning compression based on constitutive model containing dislocation density. Mechanics of Materi-
854 als 157, 103830. URL: <https://www.sciencedirect.com/science/article/pii/S0167663621000831>, doi:<https://doi.org/10.1016/j.mechmat.2021.103830>.
- 855 You, Y., Kou, X., Tan, S., 2015. Adaptive meshing for finite element analysis of heterogeneous materials. Computer-Aided
856 Design 62, 176–189. URL: <https://linkinghub.elsevier.com/retrieve/pii/S0010448514002826>, doi:[10.1016/j.cad.2014.11.011](https://doi.org/10.1016/j.cad.2014.11.011).
- 857 Zecevic, M., 2026. A green's function fast multipole method for computation of micromechanical fields in heterogeneous
858 materials. Computer Methods in Applied Mechanics and Engineering 448, 118436. URL: <https://www.sciencedirect.com/science/article/pii/S004578252500708X>, doi:<https://doi.org/10.1016/j.cma.2025.118436>.
- 859 Zhang, Q., Cha, D., Bajaj, C., 2015. Quality Partitioned Meshing of Multi-material Objects. Procedia Engineering 124,
860 187–199. URL: <https://linkinghub.elsevier.com/retrieve/pii/S1877705815032336>, doi:[10.1016/j.proeng.2015.10.132](https://doi.org/10.1016/j.proeng.2015.10.132).